Journal of Materials Chemistry A

ROYAL SOCIETY OF CHEMISTRY

REVIEW

View Article Online
View Journal | View Issue

Cite this: J. Mater. Chem. A, 2023, 11, 23720

Recent progress in polymer nanosheets for photocatalysis

Shunhang Wei, †[ab] Lei Wang,†[c] Jianyong Yue,†[d] Rong Wu,[d] Zebo Fang*[a] and Yuxi Xu *[b]

Polymers have been considered as promising photocatalysts for energy conversion and environmental remediation, because of their inherent advantages such as adjustable optical and electronic properties as well as abundant active sites. However, it is difficult for polymers without effective design to achieve ideal photocatalytic performance. Compared with bulk polymers, polymer nanosheets obtained by exfoliation have the thickness of single or multiple atomic layers, which possess numerous unique advantages, such as more accessible active sites, shorter carrier transport distances, a prolonged lifetime of photogenerated carriers and the atomic level regulation of the backbone. Therefore extensive efforts have been focused on photocatalysts based on polymer nanosheets, and remarkable progress has been reported. In this review, the principles of photocatalytic water splitting, pollutant degradation and CO_2 reduction are briefly introduced. And then recent advances in polymer nanosheets (conjugated microporous polymers, covalent organic frameworks, conjugated triazine frameworks and carbon nitrides) and their heterojunctions in the above-mentioned fields are highlighted. Specifically, the effects of the modification strategy on their light absorption ability, carrier migration, and photocatalytic activity are discussed. Finally, the important challenges and potential opportunities for developing polymer nanosheets and their heterojunctions as high-performance photocatalysts are envisaged. The insights exhibited in this review can provide a useful guidance for the design and development of polymer nanosheet based photocatalysts.

Received 7th September 2023
Accepted 16th October 2023

DOI: 10.1039/d3ta05435g

rsc.li/materials-a

1. Introduction

The energy of sunlight reaching the Earth per hour is enough to meet the energy demand of modern society per year,[1,2] thereby the efficient use of solar energy is expected to alleviate the energy crisis and environmental pollution.[3–6] Due to some inherent properties of sunlight (low energy density, intermittency, diffusion, *etc.*), converting solar energy into chemical

[a]Zhejiang Engineering Research Center of MEMS, Shaoxing University, Shaoxing 312000, China. E-mail: csfzb@usx.edu.cn
[b]School of Engineering, Westlake University, Hangzhou 310024, China. E-mail: xuyuxi@westlake.edu.cn
[c]School of Environmental Science and Engineering, Guangzhou University, Guangzhou 510006, China
[d]School of Physics Science and Technology, Xinjiang University, Urumqi 830000, China
† Equal contribution.

Shunhang Wei

Shunhang Wei received his PhD degree from Tongji University (2020) under the supervision of Prof. Xiaoxiang Xu. Currently, he works at Shaoxing University, and his research is mainly focused on low-dimensional materials and their applications in energy storage and conversion.

Zebo Fang

Zebo Fang received his PhD degree from Lanzhou University (2006). He then worked as a postdoctoral fellow at Fudan University and a visiting scholar at the City University of Hong Kong, respectively. Currently, he works at Shaoxing University as a professor, and his research is mainly focused on semiconductor materials for energy storage and conversion.

energy is considered as an effective way to improve solar energy utilization efficiency.[7–13] Inspired by photosynthesis in nature through which green plants convert carbon dioxide and water into energy-rich organic matter under mild conditions, artificial photosynthesis based on semiconductor photocatalytic technology is proposed and widely concerned. For example, photocatalytic water splitting to produce clean hydrogen fuel[14–20] and photocatalytic CO_2 reduction to produce high value-added chemicals (methane, methanol, *etc.*)[21–25] have shown great prospects in alleviating the energy crisis. In addition, solar-driven degradation of pollutants (such as volatile organic compounds, antibiotics and organic dyes) is a powerful technology to solve the problem of environmental pollution.[26–31]

Since the successful application of TiO_2 in photocatalytic water splitting,[32] a large number of inorganic photocatalysts have been explored, such as oxides ($NaTaO_3$, ZnO, and $SrTiO_3$),[33–35] sulfides (In_2S_3 and $ZnIn_2S_4$)[36–38] and oxynitrides (Ta_3N_5, $LaTiO_2N$, and $BaTaO_2N$).[39–41] Although a series of advances have been achieved in photocatalysis, they usually exhibit low quantum efficiency due to rapid carrier recombination. In addition, some of them have poor visible-light absorption ability, toxicity, photocorrosion and costly transition metals, which severely limit their large-scale applications. More importantly, the optical and electronic properties of inorganic materials can only be adjusted within a relatively limited range due to their inherent properties.[42] Therefore, it remains an urgent need to develop inexpensive, stable, harmless and structurally adjustable photocatalysts to achieve high photocatalytic performance.

Polymer photocatalysts, composed of earth-abundant light elements (C, H, N, S, *etc.*), possess excellent designability of the structure and functionality and can overcome some shortcomings of inorganic photocatalysts. Most polymer photocatalysts have visible-light absorption ability benefited from their delocalized π-system.[43] More importantly, their electronic and optical properties can be effectively regulated *via* controlling the synthesis conditions. For example, Cooper *et al.* synthesized a series of conjugated microporous polymers (CMPs) with an optical gap ranging from 1.94 eV to 2.95 eV *via* changing the monomer compositions involved in the synthesis reaction.[44] At present, carbon nitrides, covalent organic frameworks (COFs), conjugated triazine frameworks (CTFs), CMPs and linear conjugated polymers are the main polymer photocatalysts. Among them, although linear conjugated polymers are first reported,[45] their photocatalytic activity is generally poor due to the limited electron delocalization.[46] Therefore, the evolution of polymer photocatalysts mainly focuses on the other four types. To further improve the photocatalytic performance of polymers, morphology design and construction of heterojunctions are widely adopted. Compared with other morphologies, polymer nanosheets display distinctive advantages including a large specific surface area, abundant active sites and a short carrier migration distance. The construction of heterojunctions can improve various properties such as light absorption and carrier migration. Therefore single-component polymer nanosheets and polymer nanosheet-based heterojunctions are important research directions for polymer photocatalysts.

This work summarizes the research progress of COF, CTF, CMP and carbon nitride nanosheets and their heterojunctions in photocatalytic hydrogen production, CO_2 reduction and pollutant degradation (Scheme 1). Firstly, the basic rules of the above three types of photocatalytic processes and the advantages of polymer nanosheets in photocatalysis are briefly discussed. Subsequently, the current advances and optimization methods of single-component polymer nanosheets and polymer nanosheet-based heterojunctions are summarized. Finally, some beneficial guiding opinions of polymer nanosheets for photocatalysis are put forward and expected to obtain better photocatalytic activities.

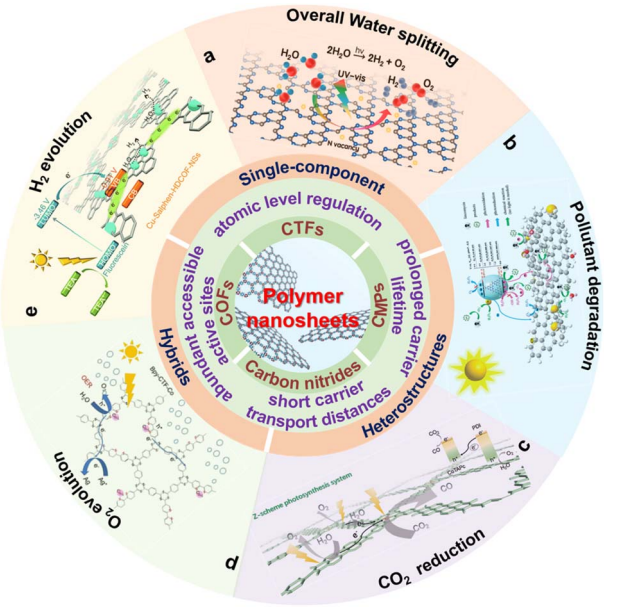

Scheme 1 Schematic illustration of the properties and photocatalytic applications for polymer nanosheets. (a) Reproduced with permission from ref. 175, © American Chemical Society 2022. (b) Reproduced with permission from ref. 176, © Wiley-VCH GmbH 2020. (c) Reprinted with permission from ref. 84, © Wiley-VCH GmbH 2022. (d) Reprinted with permission from ref. 177, © Royal Society of Chemistry 2022. (e) Reprinted with permission from ref. 148, © Royal Society of Chemistry 2020.

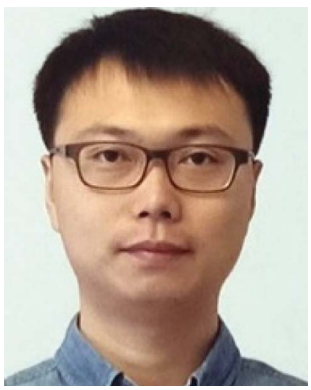

Yuxi Xu

Yuxi Xu received his B.S. degree from Wuhan University (2007) and PhD degree from Tsinghua University (2011). He then worked as a postdoctoral fellow at the University of California, Los Angeles. He joined the faculty of Fudan University in 2015 and moved to Westlake University in 2019. His research interests include chemically modified graphene, 2D polymers, and self-assembled functional materials.

2. Basic principles for photocatalytic water splitting, pollutant degradation and CO_2 reduction

Photocatalytic water splitting and CO_2 reduction convert solar energy to chemical energy (such as H_2, CH_4 and CH_3OH), which have attracted enormous attention in alleviating energy shortage and greenhouse effects. In addition, thanks to the green, efficient and secondary pollution free characteristics, photocatalytic degradation shows promising potential in pollutant removal (dye molecules, antibiotics, NO_x, *etc.*). The photocatalytic process needs to meet both dynamic and thermodynamic requirements. Photocatalytic water splitting, degradation and CO_2 reduction have the same dynamic process, as shown in Fig. 1a. First, electrons and holes are generated under irradiation. And then, some of the generated carriers will migrate to the surface active sites for a redox reaction. Meanwhile, some carriers will be recombined in the bulk and on the surface of photocatalysts. Inhibiting carrier recombination is an important means to improve photocatalytic activity, and lots of effective methods have been proposed, including doping,[47,48] constructing heterojunctions,[49–52] and loading cocatalysts.[53,54] On the other hand, thermodynamic requirements for the three photocatalytic reactions are different (Fig. 1b). For water splitting, the conduction band minimum (CBM) for H_2 production needs to locate at a more negative position than −0.41 V (*vs.* NHE, pH = 7), and the valence band maximum (VBM) location for O_2 production should more positive than 0.82 V (*vs.* NHE, pH = 7). Generally, the photocatalytic CO_2 reduction reaction is more difficult than the photocatalytic water splitting, because the high stability of CO_2 molecules requires a significant energy input for C=O bond cleavage (bond enthalpy + 805 kJ mol^{-1}).[55,56] The photogenerated electrons and holes reduce CO_2 to various products with the corresponding redox potentials (eqn (1)–(5)) and oxidize water to O_2, respectively.[57–59] For photodegradation, the photogenerated electrons and holes can directly decompose pollutants *via* redox reactions. Also, they can firstly react with O_2 dissolved in water and water molecules to form superoxide radicals ($^{\bullet}O_2^-$, −0.33 V *vs.* NHE, pH = 7),[60] hydroxyl radicals ($^{\bullet}OH$, 2.34 V *vs.* NHE, pH = 7),[61] *etc.*, and then decompose pollutants.

$$CO_2 + 2H^+ + 2e^- \rightarrow HCOOH \ -0.61 \text{ V } \textit{vs.} \text{ NHE (pH = 7)} \quad (1)$$

$$CO_2 + 2H^+ + 2e^- \rightarrow CO + H_2O \ -0.53 \text{ V } \textit{vs.} \text{ NHE (pH = 7)} \quad (2)$$

$$CO_2 + 4H^+ + 4e^- \rightarrow HCHO + H_2O \ -0.48 \text{ V } \textit{vs.} \text{ NHE (pH = 7)} \quad (3)$$

$$CO_2 + 6H^+ + 6e^- \rightarrow CH_3OH + H_2O \ -0.38 \text{ V } \textit{vs.} \text{ NHE (pH = 7)} \quad (4)$$

$$CO_2 + 8H^+ + 8e^- \rightarrow CH_4 + 2H_2O \ -0.24 \text{ V } \textit{vs.} \text{ NHE (pH = 7)} \quad (5)$$

For the three photocatalytic reactions, there are different research focuses in increasing photocatalytic performance. For example, H_2 and O_2 can combine to form water on the surface of photocatalysts, so the inhibition of the H_2–O_2 recombination reverse reaction is a research focus for photocatalytic water splitting. Several strategies have been proven to be effective, such as selective cocatalyst deposition[14] and introducing amino functional groups on the catalyst surface.[62] Some pollutants (antibiotics, *etc.*) cannot be completely degraded to non-toxic substances, so the design of photocatalysts with high redox ability based on the degradation pathway is a research focus of photocatalytic degradation. The photocatalytic CO_2 reduction reaction undergoes various intermediate steps and produces various by-products, resulting in a complex reaction mechanism and low selectivity of products. Therefore achieving efficient CO_2 conversion with high selectivity is a research focus of photocatalytic CO_2 reduction.

3. Advantages of polymer nanosheets for photocatalysis

For semiconductor photocatalysts, the morphology has an important effect on carrier migration and surface transfer. Therefore photocatalysts with different morphologies are

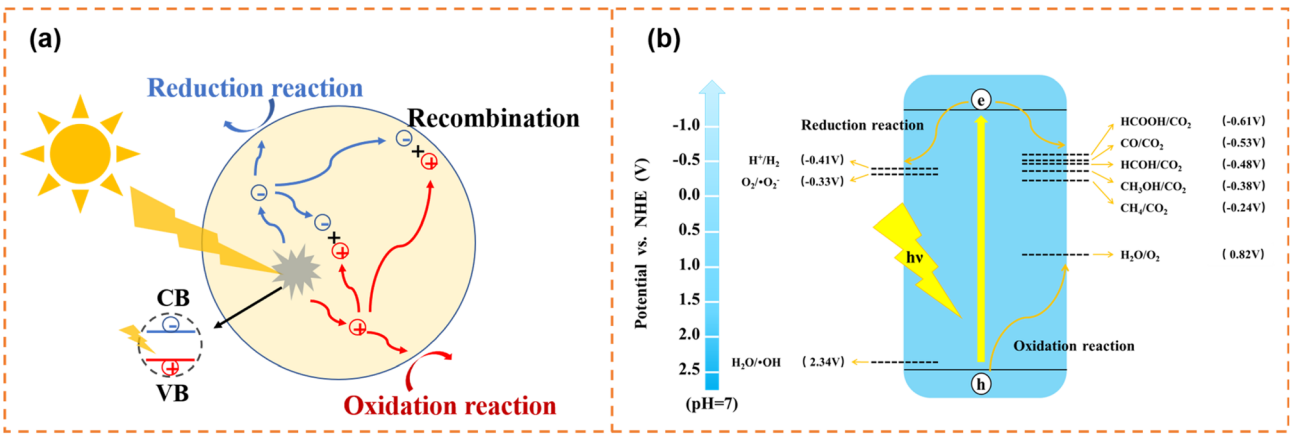

Fig. 1 (a) Schematic diagram of the photogenerated carrier transfer process. (b) Schematic illustration of thermodynamic requirements for photocatalysis.

developed to achieve excellent photocatalytic performance. Compared with other morphologies, nanosheets have a cross section that can be as large as micrometers and a thickness as thin as a single atomic layer. The wide cross section is beneficial for receiving solar photons, and the ultra-thin thickness greatly shortens the carrier migration distance. Recently, abundant polymer nanosheets with an adjustable thickness have been prepared by top-down (exfoliation method, *etc.*) or bottom-up (interface polymerization, solution polymerization, mechanochemistry, *etc.*) approaches.[46,63,64]

Modification strategies (doping, increasing active sites, *etc.*) are considered as important routes to enhance the photocatalytic performance of polymer nanosheets. Generally, the modifications in bulk photocatalysts are limited to the surface or the shallow depth below the surface because of the low ratio of surface atoms to entire material. In contrast, the thin polymer nanosheets are mostly composed of surface atoms, which can be modified adequately. More importantly, polymer nanosheets can even realize atomic-level regulation of the backbone and targeted introduction of active sites, resulting in precise and diversified modifications.[65] For example, on-surface synthesis (surface as a template to catalyze bond formation) could achieve the atomically precise design of polymer nanosheets.[66,67] Song *et al.* constructed a compact active site layout (boron atoms as the active sites) by adjusting the molecular size of monomers.[68] In addition, the band gap and electronic properties of polymers can be effectively regulated by adjusting monomer types and the conjugation degree.[69,70] In light of the above-mentioned features, polymer nanosheets show bright application prospects in the field of photocatalysis.

4. Single-component polymer nanosheets for photocatalysis

4.1 CMP photocatalysts

CMP photocatalysts are a class of amorphous polymers with an expanded π-conjugated structure and continuous networks, featuring excellent chemical and thermal stability.[71] Because CMPs can be synthesized using thousands of monomers, their band structure and active sites can be flexibly regulated.[72] Over the past decade, various CMPs have exhibited outstanding photocatalytic activity, for example, perylene-containing CMPs,[73] dibenzothiophene dioxide containing CMPs,[74] spirobifluorene-linked CMPs,[75] and dibenzothiophene-*S*,*S*-dioxide-containing CMPs.[76] Typical CMPs usually show a nanoparticle-like morphology because of the highly cross-linked network. In order to enrich the morphologies of CMPs, some effective strategies have been developed. For example, using carbon nanospheres, single-walled carbon nanotubes and reduced graphene oxide as templates can form ball-, stick- and sandwich-like CMPs, respectively.[77] Selecting toluene, p-xylene and mesitylene as solvents can obtain CMPs with sphere-, tubular- and plate-like structures, respectively.[78] Limited by the synthesis methods of CMP nanosheets, their applications in photocatalysis have been rarely reported so far. Nonetheless, some representative articles are still worth mentioning.

4.1.1 Photocatalytic water splitting

4.1.1.1 Photocatalytic H_2 production. Jiang *et al.* used 1,4-benzenediboronic acid bis(pinacol)ester (DBABz), 1,3,6,8-tetrabromopyrene (TBrPy) and 3,7-dibromodibenzothiophene-*S*,*S*-dioxide (DBrBTDO) as the π-bridge, donor and acceptor, respectively, to prepare D–π–A CMP photocatalysts (Fig. 2a).[79] D–π–A CMP nanosheets with a thickness of around 100 nm (denoted as PyBS-4) were obtained when the ratio of donor to acceptor was 15 : 85. The high content of acceptors resulted in high hydrophilicity (Fig. 2b), which was beneficial for the contact between water and the CMP photocatalyst surface. More importantly, thanks to the structural nature of D–π–A polymers, the light-induced electrons could rapidly transfer from the HOMO orbits of the donor to the LUMO orbits of the acceptor along the polymer skeleton, inhibiting photogenerated carrier recombination efficiently (Fig. 2c). Therefore the photocatalytic H_2 evolution rate of PyBS-4 reached 0.21 mmol h^{-1} under visible-light irradiation (λ > 420 nm; its dosage was 25 mg), which was higher than that of D–π–A CMP photocatalysts with other morphologies.[80]

4.1.1.2 Photocatalytic O_2 production. Xu *et al.* successfully synthesized aza-fused CMP (aza-CMP) nanosheets using 1,2,4,5-benzenetetramine tetrahydrochloride and hexaketocyclohexane octahydrate as the raw monomers.[81] The band gap of the aza-CMP nanosheets was ~1.22 eV, and their VBM potential (6.08 eV *vs.* vacuum level) far exceeded the required potential for water oxidation. Therefore, the aza-CMP nanosheets exhibited photocatalytic O_2 production activity under visible-light irradiation (λ > 420 nm; ~1.0 μmol h^{-1}) and even near infrared light irradiation (λ > 800 nm; ~0.4 μmol h^{-1}). When the aza-CMP nanosheets were further treated using the liquid exfoliation method, ultrathin aza-CMP nanosheets with a thickness of ~10 nm were obtained. Benefiting from improved photoresponsivity and more accessible reaction sites, the ultrathin aza-CMP nanosheets exhibited a three-fold enhancement in the photocatalytic O_2 production rate under visible-light irradiation.

4.1.1.3 Photocatalytic overall water splitting. Xu *et al.* employed terminal alkynes (1,3,5-tris-(4-ethynylphenyl)-benzene (TEPB) and 1,3,5-triethynylbenzene (TEB)) as raw materials to fabricate 1,3-diyne-linked CMP nanosheets.[82] The obtained CMP nanosheets prepared from TEPB (denoted as PTEPB) exhibited a single-layer or possible double-layer morphology (Fig. 2d). In contrast, the CMP derived from TEB (denoted as PTEB) was prone to form aggregated structures due to its large interlayer interaction energy (0.035 J m^{-2}) and planar molecular structure. Thanks to the role of 1,3-diyne covalent linkage in tuning band structures, both PTEPB and PTEB exhibited narrow band gaps (~2.85 eV and ~2.94 eV, respectively). And their VBM and CBM positions satisfied the thermodynamic requirements for water splitting. Therefore they exhibited stable photocatalytic overall water splitting activity under visible-light irradiation. Theoretical calculations further revealed the possible reactive sites for water oxidation (Fig. 2e and f): the O_2 evolution for PTEPB could occur spontaneously under visible-light irradiation *via* a dual-site process, while both

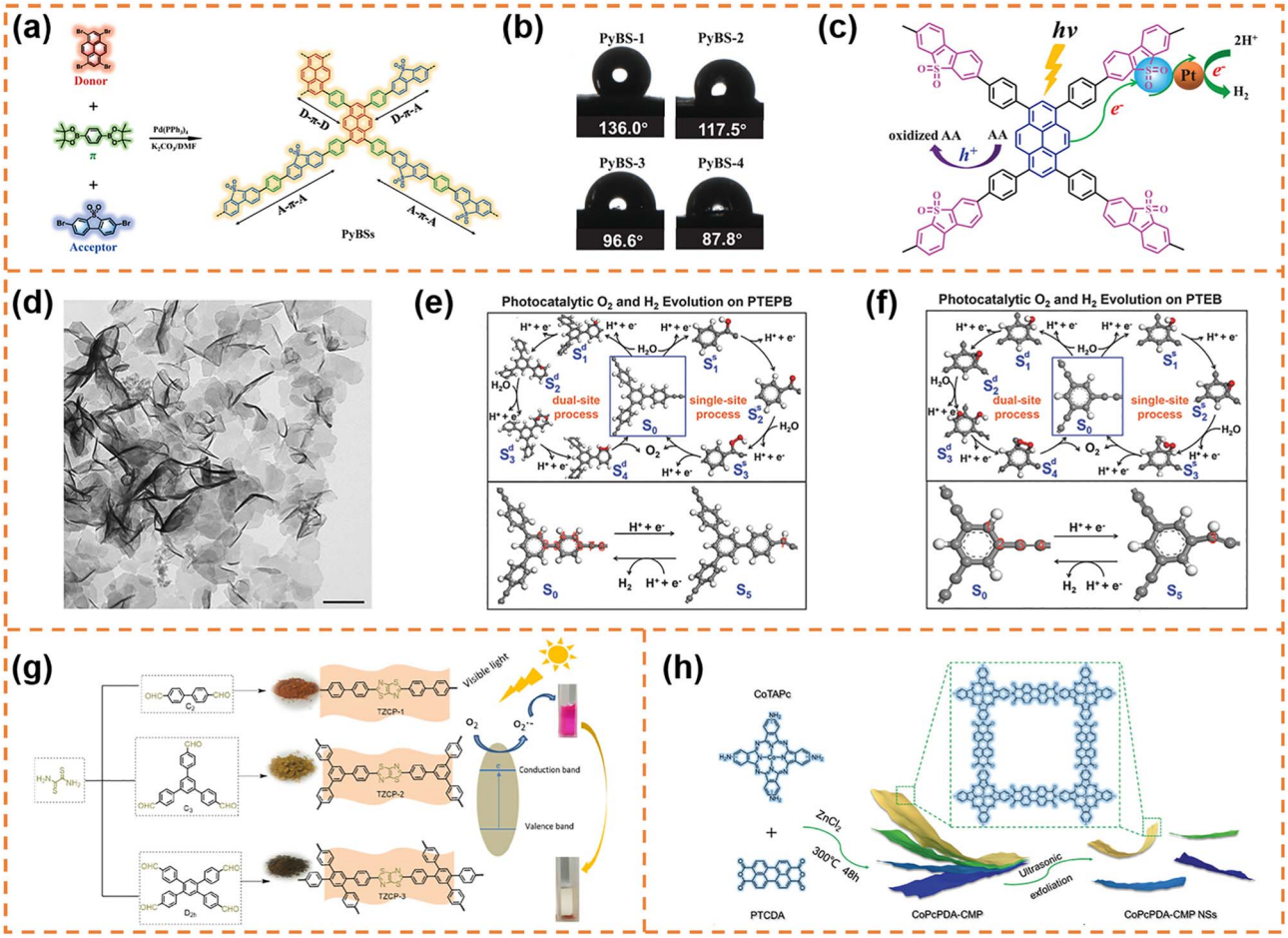

Fig. 2 (a) The synthesis of the D–π–A containing copolymer photocatalysts with the notional polymer structure. (b) Water contact angles for the copolymers. (c) The proposed photocatalytic mechanism of the D–π–A copolymer photocatalyst. Reprinted with permission from ref. 79, © Wiley-VCH GmbH 2021. (d) TEM image of PTEPB. Proposed photocatalytic cycles of the oxygen evolution reaction (*via* single-site and dual-site processes) and hydrogen evolution reaction with the energetically most feasible active sites in both PTEPB (e) and PTEB (f). Reprinted with permission from ref. 82, © Wiley-VCH GmbH 2017. (g) Synthetic routes of the TzTz-based conjugated porous polymers. Reprinted with permission from ref. 83, © American Chemical Society 2019. (h) Schematic illustration of CoPcPDA-CMP NS synthesis. Reprinted with permission from ref. 84, © Wiley-VCH GmbH 2022.

single-site and dual-site processes might take place for PTEB. Benefiting from the ultrathin thickness and reactive sites, the average H_2 production rate of PTEPB (218 μmol h^{-1} g^{-1}) was better than that of PTEB (102 μmol h^{-1} g^{-1}). These findings provided a new insight into designing and synthesizing CMP nanosheets for photocatalytic overall water splitting.

4.1.2 Photocatalytic degradation. Jin *et al.* synthesized a series of thiazolo[5,4-*d*] thiazole (TzTz)-linked CMP nanosheets *via* incorporating a TzTz unit and polyphenyl molecules with C_2, C_3, and D_{2h} symmetric groups (Fig. 2g).[83] These CMPs were denoted as TZCP-1, TZCP-2 and TZCP-3 based on the symmetric groups, respectively. The introduction of the heteroatom-S/N and conjugated structure resulted in three samples with different colors (red TZCP-1, green TZCP-2 and deep-green TZCP-3) and specific surface areas (110 m^2 g^{-1} for TZCP-1, 385 m^2 g^{-1} for TZCP-2 and 673 m^2 g^{-1} for TZCP-3), which indicated that the change of building blocks could tune physical characteristics. The monolayer thicknesses of TZCP-1, TZCP-2, and TZCP-3 were around 4.1, 4.4 and 4.8 nm, respectively. TZCP-1 and TZCP-3 exhibited the largest sheets and a uniform smallest sheet morphology, respectively, indicating that the geometry of the aldehyde monomers had a direct impact on the morphology of the polymers. The high specific surface area and small size of layers could improve the interaction area between catalysts and dyes, which benefited the photocatalytic degradation activity. Therefore, TZCP-3 had the highest photodegradation rate under visible-light irradiation (completely degraded RhB in 30 min and degraded 80% MO in 60 min).

4.1.3 Photocatalytic CO_2 reduction. Jiang *et al.* used tetraaminophthalocyanatocobalt(II) (CoTAPc) and 3,4,9,10-perylenetetracarboxylic dianhydride (PTCDA) as raw materials to prepare bulk imide-based covalent organic polymer CoPcPDA-CMP, and further exfoliated it into CoPcPDA-CMP nanosheets with a thickness of ~5 nm (Fig. 2h).[84] The CoPcPDA-CMP nanosheet itself constructed a Z-scheme system, in which

cobalt phthalocyanine (CoPc) moieties were used for CO_2 reduction and 3,4,9,10-perylenetetracarboxylic diimide (PDI) moieties were used for H_2O oxidation. In the CoPcPDA-CMP nanosheet, the CoPc and PDI moieties were integrated through an imide ring. The CO formation rate for bulk CoPcPDA-CMP is almost two times faster than that for the mixture of CoTAPc and PDI (1 : 2), indicating that the unique structure is beneficial for electron–hole separation. When the bulk CoPcPDA-CMPs were exfoliated into nanosheets, the exposed active sites were obviously increased and the electron transfer process was more efficient, so that the CoPcPDA-CMP nanosheets exhibited a faster CO formation rate (14.27 μmol g^{-1} h^{-1}) and a higher CO selectivity (92%) under visible-light irradiation. This work developed a new high-performance CMP nanosheet photocatalyst for CO_2 conversion with H_2O as an electron donor, which was competitive to the state-of-the-art visible-light-driven organic photocatalysts for overall CO_2 reduction.

4.2 COF photocatalysts

COFs are a class of highly crystalline porous polymers with a high specific surface area, abundant active sites and chemical stability.[85] Their light absorption ability can be adjusted by modifying building blocks. In addition, their highly ordered structures and strong interlayer interactions provide unique advantages in separation of photogenerated carriers.[86] Therefore, COFs have great application potential in photocatalysis.

The preparation strategies of COF nanosheets can be classified into top-down and bottom-up strategies.[87] The top-down strategy aims to exfoliate a bulk polymer into single- or multilayer nanosheets *via* utilizing external forces to break the weak interlayer interactions. So far, the well-developed exfoliation strategies generally include sonication exfoliation, chemical exfoliation, mechanical exfoliation and self-exfoliation. For example, Dichtel *et al.* exfoliated a hydrazone-linked COF into bulk quantities of two-dimensional (2D) polymer nanosheets by immersing in several common laboratory solvents (THF, dioxane, MeOH, *etc.*).[88] Tsuru *et al.* prepared COF-1 nanosheets by ultrasonic exfoliation through dispersing COF-1 powder in dichloromethane.[89] Banerjee *et al.* used a mechanical grinding route to obtain graphene-like layered COF nanosheets.[90] The bottom-up methods are usually realized *via* interfacial synthesis (such as liquid–liquid interface and gas–liquid interface). For example, Zhang *et al.* prepared an imine-linked covalent organic monolayer at the air–water interface.[91] Ma *et al.* synthesized high-quality COF nanosheets at the interface of two miscible organic solvents.[92] It is worth noting that reports of COF nanosheets for photocatalysis are still rare, which may be ascribed to the limited synthesis methods.[93–95] Herein, the relevant important developments of COF nanosheets in photocatalysis are discussed.

4.2.1 Photocatalytic water splitting

4.2.1.1 Photocatalytic H_2 production. Osakada *et al.* used a liquid-phase exfoliation method to obtain thin-layered porphyrin-comprised COF nanosheets (denoted as e-CON) in common solvents (dichloromethane, methanol, pyridine, nitrobenzene and H_2O).[96] Compared with other solvents, the surface energy of H_2O (102.8 mJ m^{-2}) was closer to that of bulk porphyrin-comprised COFs (DhaTph) (106.6 mJ m^{-2}), so the porphyrin-comprised COFs could be easily exfoliated in H_2O (denoted as e-CON(H_2O)). The produced e-CON(H_2O) had a thickness of 1–2 nm and a width of 50–60 nm. Using Pt/RGO as the co-photocatalyst and methanol as the sacrificial agent, its photocatalytic H_2 yield rate was nearly five times higher than that of unexfoliated DhaTph. Cooper *et al.* used 3,9-diaminobenzo[1,2-*b* : 4,5-*b*′]bis[1]benzothiophene sulfone (FSA) as the monomer to produce FS-COF *via* a Schiff-base condensation reaction.[97] It could be partially exfoliated into thin stacks with thicknesses of 5–25 nm. Using ascorbic acid as the sacrificial agent and Pt as the co-catalyst, its photocatalytic H_2 yield rate reached 10.1 mmol g^{-1} h^{-1} under visible-light irradiation (λ > 420 nm), which was ~6.5 times higher that that of TP-COF (synthesised using 4,4″ diamino-*p*-terphenyl as the monomer). Besides the longer absorption edge and higher BET surface area, the authors believed that the partial exfoliation of FS-COF also contributed to the improved photocatalytic performance because the nanosheet-like morphology could provide more active sites for hydrogen evolution.[98,99]

4.2.1.2 Photocatalytic overall water splitting. Lan *et al.* exfoliated three β-ketoamine COFs (TpBD-COF with biphenyl units, and TpBpy-COF and TpBpy-2-COF with a bipyridine structure) to obtain nanosheets (NSs) with a thickness of 3–4 nm *via* a "top-down" route, and then *in situ* incorporated 1.19–1.28 wt% ultra-small Pt nanoparticles (around 1.1 nm) co-catalyst into their open channels (Fig. 3a–c).[100] The obtained samples were denoted as Pt@ TpBD-NS, Pt@TpBpy-NS and Pt@TpBpy-2-NS, respectively. Except Pt@TpBD-NS, both Pt@TpBpy-NS and Pt@TpBpy-2-NS exhibited overall water splitting activity. The H_2 and O_2 evolution amounts in 5 h under visible-light irradiation for Pt@TpBpy-NS were 9.9 and 4.8 μmol, respectively, and those for Pt@TpBpy-2-NS were 3.1 and 1.4 μmol. The different photocatalytic performance indicated that the bipyridine structure and the position of N sites in the heterocyclic ring were important for overall water splitting. Control experiments using bulk COFs without a nanosheet morphology and post-loading Pt on COF NSs confirmed that the nanosheet morphology and ultra-small Pt NPs uniformly distributed in the pores of COFs were key factors for enhancing the water splitting activity. DFT theoretical calculation (Fig. 3d–f) further indicated that the electron transfer from the Bpy to the Tp section was more efficient in TpBpy-NS than that in TpBpy-2-NS, and C2d was the optimal oxygen evolution reaction path.

4.3 CTF photocatalysts

CTFs are composed of covalent and aromatic triazine linkages, possessing high pore density, rich active sites and chemical and thermal stability. Currently, most of the reported CTFs are amorphous or semicrystalline. Although CTFs have an intrinsically 2D layered structure, the π–π interaction between layers generally results in the formation of bulk CTFs. The long charge diffusion distance, abundant defects and boundaries in bulk CTFs seriously restrict photocatalytic performance. In order to

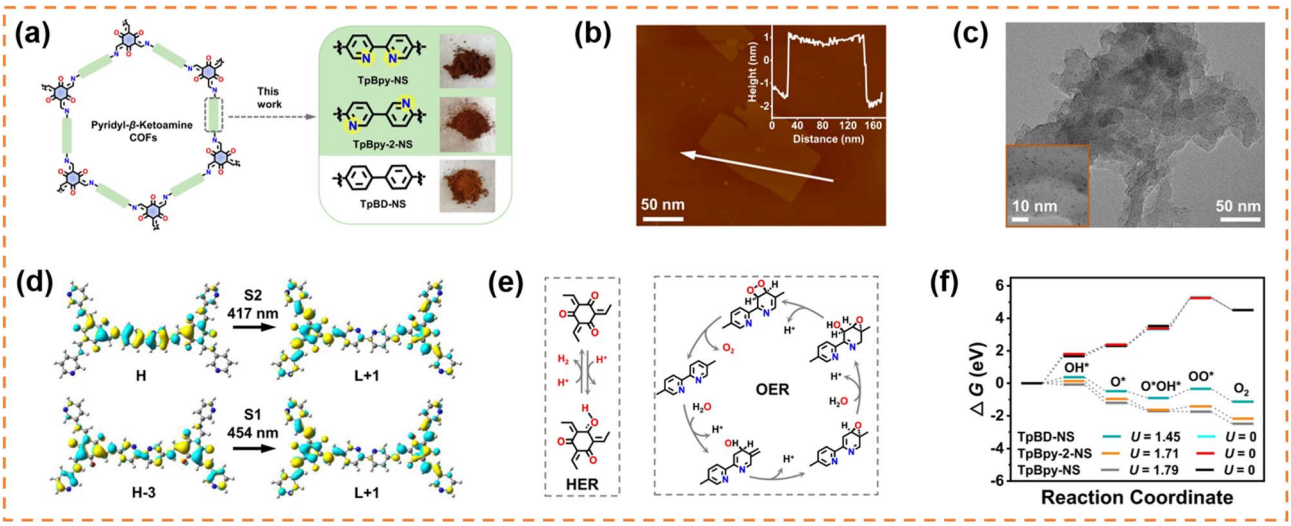

Fig. 3 (a) β-Ketoamine COFs with the same topology and similar atomic composition. (b) AFM image and (c) TEM image of Pt@TpBpy-NS. (d) The TD-DFT calculated electronic transition of TpBpy-NS. (e) The possible process of the HER on the Tp segment and the OER *via* a dual-site process on the Bpy segment in TpBpy-NS. (f) The comparison of calculated Gibbs free energy change for C2d paths of the OER for TpBD-NS, TpBpy-2-NS and TpBpy-NS at pH = 7. Reprinted with permission from ref. 100, © The Author(s) 2023.

synthesize CTF nanosheets, different strategies have been developed, including chemical exfoliation, interfacial polymerization, mechanical exfoliation and monomer-dependent synthesis.[101] For example, Fan *et al.* utilized an acid-base driven intercalation reaction to obtain 1–2 layered CTF nanosheets.[102] Xu *et al.* exfoliated bulk CTFs into micrometer-size few-layer CTF nanosheets with a thickness of 2–3 nm through micromechanical cleavage and liquid sonication.[103] Wang *et al.* used a ball mill strategy to break the interlayer π–π interactions of bulk perfluorinated CTFs and obtain ultrathin nanosheets with a thickness of ~4.2 nm.[104]

4.3.1 Photocatalytic water splitting

4.3.1.1 Photocatalytic H_2 production. Xu *et al.* prepared layered crystalline CTF powders using terephthalonitrile as the monomer and CF_3SO_3H as the catalyst.[105] The obtained layered crystalline CTFs were treated with sulfuric acid so that they were exfoliated into nanosheets containing amide groups and oxygen-containing groups (o-CTFNSs) through a rapid exothermic effect formed by adding water into the mixture containing sulfuric acid. Finally, these oxygen-containing groups were reduced using hydrazine hydrate to obtain amide-functionalized CTF nanosheets with an ultrathin thickness of ~1.5 nm (Fig. 4a–c). The amide functional groups served as electron donors, which could adjust the band gap and promote charge separation. The photocatalytic H_2 yield rate of the amide-functionalized CTF nanosheets could reach 512.3 μmol h^{-1} under visible-light irradiation, which was around 17 times higher than that of pristine layered crystalline CTFs (Fig. 4d). More importantly, the amide-functionalized CTF nanosheets have an apparent quantum yield of 11.3% at 420 nm and excellent photostability for photocatalytic H_2 evolution. Afterwards, Xu's group focused on scalable production of high-quality CTF nanosheets for photocatalytic H_2 evolution.[106,107] For example, CF_3SO_3H catalysts were employed to absorb microwave energy, which could exclusively transfer energy to the nitrile-based monomers (1,3,5-tricyanobenzene, 1,4-dicyanobenzene and 4,4′-dicyano-1,1′-biphenyl) under solvent-free conditions to facilitate a continuous cyclotrimerization reaction (Fig. 4e).[106] The microwave-assisted synthetic route can obtain a series of highly crystalline layered CTFs with the hundred-gram level in a short time (within 20 minutes). Abundant crystalline single-layer/few-layer CTF nanosheets with a thickness of 0.6–3 nm could be obtained after simple ball-milling exfoliation of the above bulk layered crystalline CTFs (Fig. 4g and h). The photocatalytic hydrogen evolution rate of the CTF nanosheets reached up to 7971 μmol g^{-1} h^{-1}, which was nearly five times higher than that of bulk CTFs. Such high photocatalytic performance could be ascribed to the more accessible active sites and higher carrier separation efficiency of exfoliated nanosheets. In the subsequent research, bulk layered crystalline CTFs were further homogeneously mixed with a sodium 1-pyrenebutyrate (PB) aqueous solution.[107] The PB molecules could spontaneously adsorb on the surface and interlayer edges of the bulk CTF, and the introduced negative charges enhanced interlayer repulsion of the CTF layers (Fig. 4i). Under mechanical ball-milling treatment, the formed shear force slipped the 2D triazine layers of the bulk CTFs into CTF nanosheets (PB-modified 2D-TP) on a large scale in water (Fig. 4j). The adsorbed PB caused a molecular doping effect on the CTF nanosheets, resulting ineffective carrier separation. The interaction between 2D-TP and PB formed a strong built-in electric field, which also accelerated photogenerated charge separation and transfer. Therefore, the photocatalytic H_2 yield rate of the PB-modified 2D-TP nanosheets (50 mg dosage) reached 1249 μmol h^{-1} under visible-light irradiation, which was 24-fold improvement in comparison with that of the bulk CTFs (Fig. 4k). In addition, they found a new solvent-free salt-catalyzed nitrile cyclotrimerization process, which could result

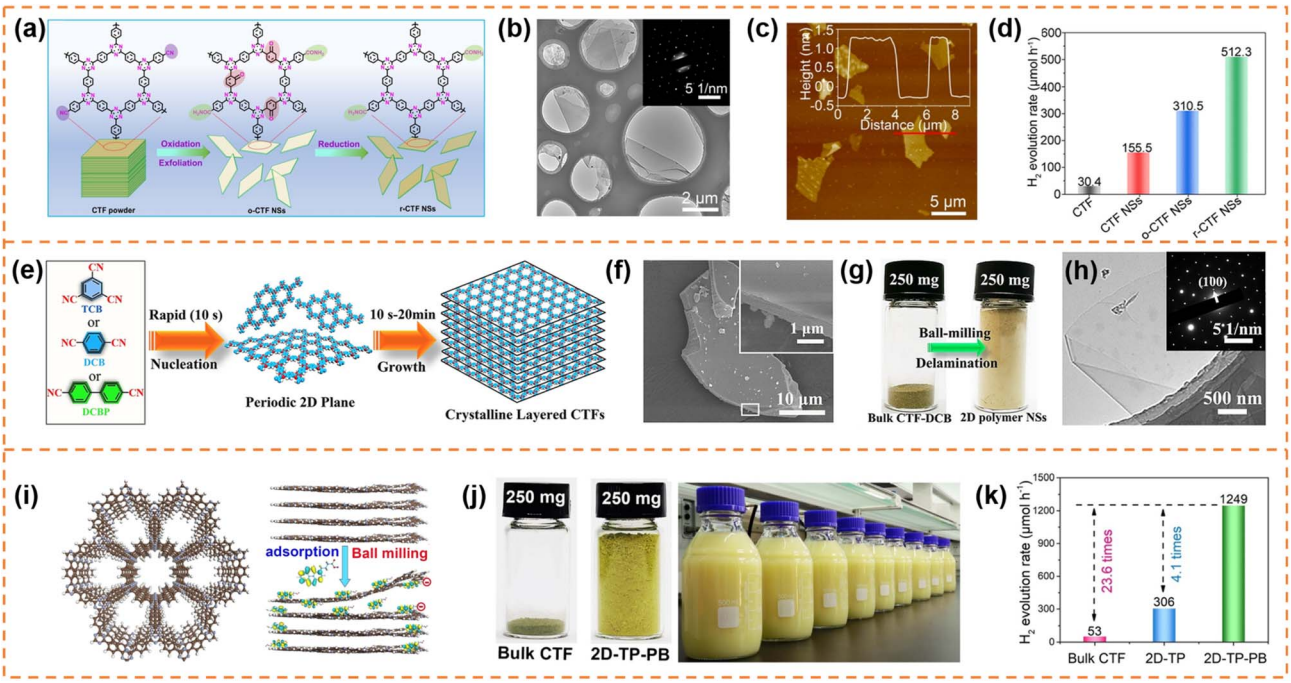

Fig. 4 (a) Schematic illustration of the redox exfoliation process. TEM image (b) and AFM image (c) of r-CTF NSs. (d) Photocatalytic H_2 evolution rates of the obtained samples. Reprinted with permission from ref. 105, © Wiley-VCH GmbH 2021. (e) The rapid synthetic route and polymerization mechanism. (f) SEM image of layered crystalline CTF-DCB. (g) Photograph of bulk CTF-DCB and the exfoliated 2D triazine polymer NSs. (h) TEM image of 2D triazine polymer NSs. Reprinted with permission from ref. 106, © Wiley-VCH GmbH 2022. (i) Schematic illustration of the adsorption of PB molecules on the surface of the CTF layer and the simultaneous exfoliation process. (j) The photograph of the bulk CTF and the corresponding exfoliated 2D-TP-PB, and scalable aqueous dispersion of 2D-TP-PB nanosheets with a concentration of 5 mg mL^{-1}. (k) Photocatalytic hydrogen evolution rate comparison at a photocatalyst loading of 50 mg. Reprinted with permission from ref. 107, © Wiley-VCH GmbH 2023.

in the formation of atomic-thin CTF nanosheets on a large scale (Fig. 5a).[108] Common salts (KCl, *etc.*) could not only facilitate the formation of a nanosheet morphology but also act as a kind of green solid catalyst to catalyze the cyclotrimerization reaction of carbonitrile monomers. The obtained crystalline CTF nanosheets (CTF NSs) with a thickness of ~80 nm could be further exfoliated into single-layer crystalline 2D triazine polymers (2D-TPs) with a thickness of ~0.6 nm *via* simple liquid ultrasonication. The obtained atomic-thin 2D-TPs with a suitable band structure and rich triazine active groups exhibited an excellent photocatalytic H_2 evolution rate (1321 μmol h^{-1}) under visible-light irradiation.

Fan *et al.* synthesized few-layer CTF nanosheets using H_2SO_4 and $(NH_4)_2S_2O_8$ as an intercalant and mild oxidant, respectively, to intercalate and exfoliate bulk CTFs (Fig. 5b).[109] The defect states introduced by exfoliation could improve visible-light absorption and suppress the radiative electron–hole recombination. Besides, the ultrathin structure could shorten the diffusion length of the photoexcited carriers and expose more active sites. Under optimum conditions, the exfoliated CTF nanosheets exhibited a high H_2 production rate (1527 μmol h^{-1} g^{-1}) under visible-light irradiation, which was much better than that of bulk CTFs. Afterwards, Fan *et al.* firstly obtained thin CTF-1 nanosheets (denoted as E-CTF) using the above exfoliation method, and then obtained protonated CTF-1 nanosheets (P-CTF) through the reaction of E-CTF with H_3PO_4 (Fig. 5c).[110] The protonation could improve the interaction among the P-CTF, H_2O molecules and Pt co-catalyst, thus facilitating the transfer of the photogenerated electrons from the Pt co-catalyst to the H_2O (Fig. 5d and e). Therefore, in the presence of a Pt (3 wt%) co-catalyst and triethanolamine sacrificial agent, the photocatalytic H_2 production rate of P-CTF (6595 μmol g^{-1} h^{-1}) under AM 1.5 irradiation was higher than that of E-CTF (3972.5 μmol g^{-1} h^{-1}) and bulk CTF-1 (810 μmol g^{-1} h^{-1}).

4.3.1.2 Photocatalytic O_2 production. The amide-functionalized CTF nanosheets prepared by Xu *et al.* also showed a better photocatalytic O_2 production rate (12.37 μmol h^{-1}) than the corresponding bulk CTFs (0.52 μmol h^{-1}) under visible-light irradiation (Co^{2+} and $AgNO_3$ served as a co-catalyst and sacrificial agent, respectively).[105] Besides the advantages of amide functional groups and morphology, the more positive VBM potential of the amide-functionalized CTF nanosheets resulted in adequate thermodynamic driving force, which was also an important reason for the enhanced photocatalytic water oxidation performance.

4.3.1.3 Photocatalytic overall water splitting. High crystallinity and hydrophilicity are the key factors to obtain photocatalytic overall water splitting activity. Besides the amide-functionalized CTF nanosheets and atomically thin crystalline 2D-TPs prepared by Xu *et al.*[105,108] the crystalline CTF nanosheets with high hydrophilicity (denoted as CTF-HUST-A1) prepared by Jin *et al.* also exhibited photocatalytic overall water splitting

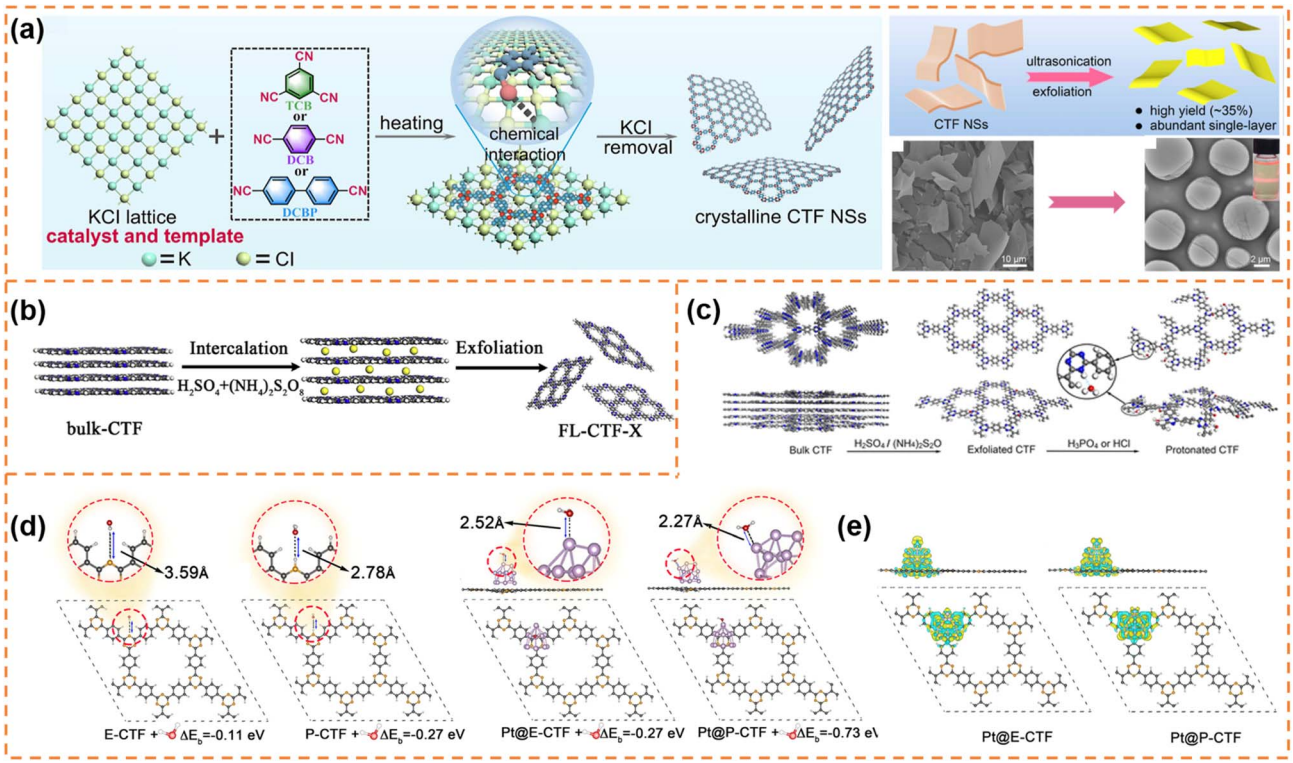

Fig. 5 (a) Proposed salt-catalytic method based on the chemical interaction between the salt lattice and carbonitrile monomers during the polymerization process, SEM image of CTF-DCB NSs and TEM image of 2D-TPs with the inset showing the Tyndall effect of 2D-TP dispersion. Reprinted with permission from ref. 108, © American Chemical Society 2023. (b) Illustration of the preparation of exfoliated CTF nanosheets. Reprinted with permission from ref. 109, © Elsevier B.V. 2020. (c) Schematic diagram of protonation modification of CTF-1. (d) Optimized configurations for E-CTF-1, P-CTF, Pt@E-CTF and Pt@P-CTF after binding with a H_2O molecule. (e) Differential charge density for Pt@E-CTF and Pt@P-CTF. Reprinted with permission from ref. 110, © American Chemical Society 2022.

activity.[111] The crystalline CTF-HUST-A1 nanosheets were synthesized using *p*-xylylenediamine as the monomer and a strong base as the catalyst. Among various base reagents (K_2CO_3, KOH, EtOK and ^{t}BuOK), the CTF-HUST-A1 synthesized in ^{t}BuOK (denoted as CTF-HUST-A1-^{t}BuOK) showed the highest crystallinity and BET surface area (644 $m^2\ g^{-1}$). The CTF-HUST-A1-^{t}BuOK nanosheets had a thickness of around 5 nm. Structures analysis showed that the –C=O groups (formed by the hydrolysis of the –C=N– groups or the oxidation of the benzylamine groups under alkaline conditions) and the –C–O–H groups (formed from the –C–NH_2 groups or by further hydrolysis of the –C=O or –C=NH groups under alkaline conditions) were the major reason for the good hydrophilicity. In addition, the high surface area and the layer structure might also partially contribute to the high hydrophilicity. The high crystallinity could inhibit the recombination of photogenerated charge carriers, the thin nanosheets could provide a shortcut for the photo-generated charges to the surface and the high hydrophilicity could promote interactions between the CTF nanosheets and water. Their synergistic roles resulted in a good overall water splitting activity (25.4 mmol g^{-1} h^{-1} and 12.9 mmol g^{-1} h^{-1}) under visible-light irradiation ($\lambda > 420$ nm) of CTF-HUST-A1-^{t}BuOK with 4.5 wt% NiP_x and 3.0 wt%Pt as dual cocatalysts.

4.4 Carbon nitride photocatalysts

Carbon nitrides are star semiconductors in the field of photocatalysis due to the advantages of easy preparation, low cost, non-toxicity, stable physical and chemical properties and suitable band structure. Carbon nitrides have different allotropes, among which graphitic carbon nitride (g-C_3N_4) is the most stable.[112,113] Recently, g-C_3N_4 with an amorphous, semi-crystalline or highly crystalline structure has been widely reported. Since Wang's pioneering report showed that g-C_3N_4 possessed photocatalytic H_2 and O_2 production activity,[114] it has been extensively studied in different photocatalytic applications (CO_2 reduction, pollutant degradation, hydrogen peroxide production, *etc.*).[115–118] However, bulk g-C_3N_4 exhibits low charge carrier separation efficiency and a small surface area, resulting in poor photocatalytic activity.[119,120] Therefore g-C_3N_4 photocatalysts with different morphologies (nanosheets,[121,122] hollow spheres,[123,124] nanofibers[125] and nanotubes[126,127]) have been developed to enhance photocatalytic performance. Among them, g-C_3N_4 nanosheets have attracted much attention due to the advantages of a high specific surface area, short diffusion length of photogenerated carriers and abundant accessible active sites.[113] g-C_3N_4 has been extensively reviewed in the field of photocatalysis.[53,112,128–135] Here, we provide a brief summary of

the photocatalytic properties of exfoliated ultrathin g-C_3N_4 nanosheets.

4.4.1 Photocatalytic water splitting

4.4.1.1 Photocatalytic H_2 production. Fang *et al.* used a liquid-phase ultrasonic exfoliation method to prepare mesoporous few-layer g-C_3N_4 nanosheets.[136] Compared with bulk g-C_3N_4, the g-C_3N_4 nanosheets possessed a higher specific surface area, abundant mesopores and a narrower bandgap. Therefore a high hydrogen evolution rate (97.6 μmol h^{-1} g^{-1}) of the g-C_3N_4 nanosheets under visible-light irradiation was achieved, which was 3.3 times higher than that of bulk g-C_3N_4. Kang *et al.* prepared g-C_3N_4 nanosheets with a thickness of ~4 nm by the hydrothermal exfoliation method (NaClO as the exfoliation agent) (Fig. 6a).[137] The simultaneous Na^+ intercalation and ClO^- oxidation resulted in the formation of abundant in-plane holes on g-C_3N_4 nanosheets, which accelerated the cross-plane diffusion of photogenerated carriers. Thanks to the inherent advantages of exfoliated nanosheets and the holey structure, the hydrogen evolution rate of the g-C_3N_4 nanosheets reached 0.89 mmol g^{-1} h^{-1}, which was 9 times higher than that of bulk g-C_3N_4. The photocatalytic activity can be further enhanced by introducing element doping during the preparation of ultrathin nanosheets. For example, Xu *et al.* prepared ultrathin g-C_3N_4 nanosheets co-doped with S, P and O non-metal atoms by a thermal-assisted exfoliation method (Fig. 6b).[138] The exfoliation resulted in an increase in the specific surface area (almost 2 times that of bulk g-C_3N_4) and more exposure of active sites, which was beneficial for photocatalysis. Upon elemental doping, S atoms occupied the interstitial sites, and P and O atoms replaced the C and N atoms, respectively, resulting in the formation of an O–P–C–N_2–S–N_2' (or N_2'–S–N_2–C_1–P–O) chain between two adjacent heptazine units (Fig. 6c). The chain as a more favorable charge transfer pathway significantly enhanced photo-induced charge transfer and separation. Therefore, the multi-atom doping and ultrathin nanosheet morphology remarkably enhanced the photocatalytic H_2 production rate (2480 μmol g^{-1} h^{-1}) under visible-light irradiation, which was about 5.3 times that of pure g-C_3N_4. Zhang *et al.* firstly prepared ultrathin g-C_3N_4 nanosheets doped with O atoms (denoted as O–CNS) by the oxygen etching method, and then incorporated P into the basal plane of g-C_3N_4 (Fig. 6d–g). Finally, oxygen and phosphorus dual-doped ultrathin g-C_3N_4 nanosheets (denoted as O, P–CNS) with a thickness of about 2.5–3.0 nm were obtained.[139] The O, P–CNS with enhanced electronic conductivity and an activated basal plane exhibited a superior H_2 generation rate of 8.7 mmol g^{-1} h^{-1} under visible-light irradiation.

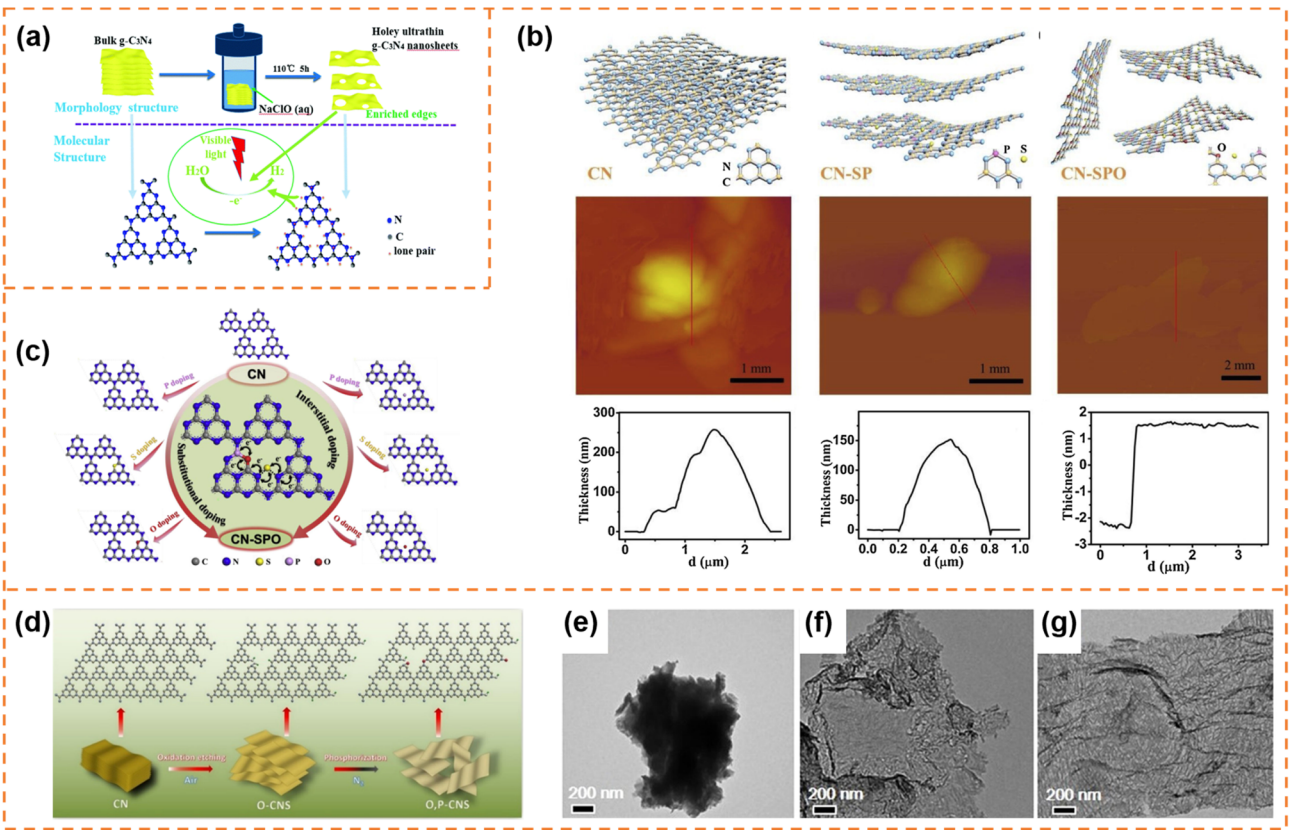

Fig. 6 (a) Schematic illustration of the NaClO (aq) hydrothermal exfoliation of bulk g-C_3N_4 into single-layer nanosheets for the photocatalytic H_2 evolution. Reprinted with permission from ref. 137, © Royal Society of Chemistry 2018. (b) Schematic illustration of the exfoliation procedure of g-C_3N_4 from CN to CN-SP and CN-SPO, and corresponding AFM images and height profile. (c) Schematic illustration of P (or S/O) doped monolayer g-C_3N_4 atomic structures with substitutional-doped sites (left), interstitial-doped sites (right) and the pathway for electron transport (middle). Reprinted with permission from ref. 138, © Elsevier B.V. 2019. (d) Fabrication process of O, P–CNS. (e–g) TEM images of CN, O–CNS and O, P–CNS. Reprinted with permission from ref. 139, © American Chemical Society 2020.

4.4.1.2 Photocatalytic overall water splitting. Bao *et al.* used a femtosecond pulsed laser to exfoliate bulk g-C_3N_4 into ultrathin nanosheets with a thickness of ~2 nm (Fig. 7a).[140] The femtosecond laser pulses broke the strong C–N covalent bonds and cleaved the *s*-triazine units as well, forming abundant –C≡N defects on the ultrathin g-C_3N_4 nanosheet surface. These cyano (–C≡N) defects not only favored the anchoring of Pt atoms but also shifted down the band edge positions. Meanwhile, the atomically dispersed Pt provided abundant active sites for the surface reaction and inhibited the back-oxidation of H_2. In addition, the more positive valence band edge position enhanced the water oxidation ability of the holes. Therefore the laser-exfoliated g-C_3N_4 nanosheets with Pt cocatalysts achieved overall water splitting activity (42.6 μmol g^{-1} h^{-1} for H_2 and 18.7 μmol g^{-1} h^{-1} for O_2; Fig. 7b).

4.4.2 Photocatalytic degradation. Yang *et al.* used different exfoliation strategies (such as thermal, chemical, ultrasonic and one-step exfoliation) to prepare ultrathin g-C_3N_4 nanosheets for photocatalytic degradation.[141] Among them, ultrathin g-C_3N_4 nanosheets obtaining by one-step exfoliation exhibited a high specific surface area, optimal band structure and high charge separation efficiency. It showed the best bisphenol A (BPA) photodegradation efficiency under visible-light irradiation, which was 6.5 times that of bulk g-C_3N_4. Mao *et al.* and Jia *et al.* also demonstrated that wet ball milling and gas bubble exfoliation methods were efficient methods to obtain thin g-C_3N_4 nanosheets for photodegradation.[142,143] Although the two methods could quickly obtain thin g-C_3N_4 nanosheets on a large scale, their improvement in photodegradation efficiency was relatively limited (2~2.5 times that of bulk g-C_3N_4).

Due to the quantum size effect, the bandgap of g-C_3N_4 nanosheets was generally widened after exfoliation. Exfoliation-induced element doping was an efficient method to enhance visible-light absorption ability and photodegradation activity. For example, Li *et al.* introduced $(NH_4)_2S_2O_8$ (APS) into the thermal exfoliation approach to prepare O-doped g-C_3N_4 nanosheets (Fig. 7c).[144] The method realized the synchronization control of the electronic structure and morphology. Due to the enlarged specific surface area, more accessible active edges, narrowed bandgap and efficient carrier separation, the O-doped g-C_3N_4 nanosheets showed 1.6 times higher photocatalytic RhB degradation activity than bulk g-C_3N_4. More importantly, RhB was completely decomposed into small inorganic salt molecules (Fig. 7d). Kim *et al.* used ammonium salts (NH_4Br) and melamine as raw materials to prepare Br-doped g-C_3N_4 nanosheets *via* a one-step exfoliation method (Fig. 7e).[145] Br doping increased the visible-light absorbance and inhibited photogenerated carrier recombination, which resulted in an increase in the degradation performance of OTC antibiotics from 30% of bulk g-C_3N_4 to 76% of Br-doped g-C_3N_4 nanosheets under visible-light irradiation for 2 h (Fig. 7f).

4.4.3 Photocatalytic CO_2 reduction. Ye *et al.* obtained atomically protonated porous g-C_3N_4 nanosheets with a thickness of ~1 nm (denoted as P–PCNNS) through protonation exfoliating with phosphoric acid (H_3PO_4).[146] Abundant micro- and meso-pores were formed on P–PCNNS, which were beneficial for exposing more active catalytic sites and facilitating the

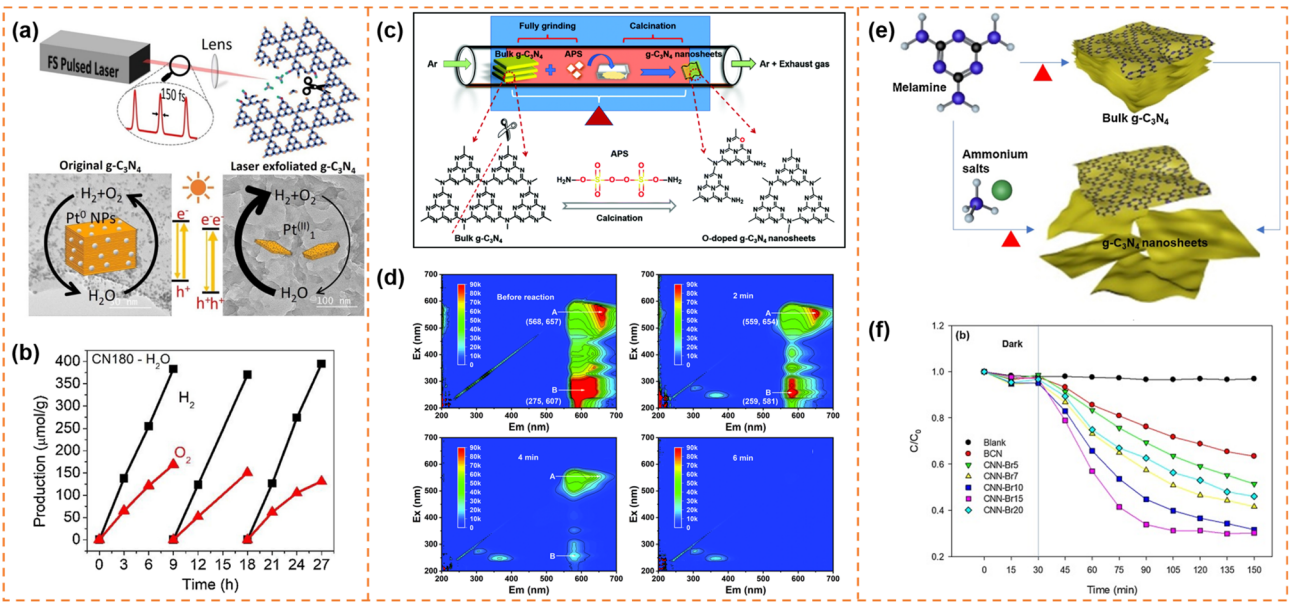

Fig. 7 (a) Illustration of the formation process of g-C_3N_4 nanosheets *via* the femtosecond laser pulse method and their photocatalytic mechanism. (b) The photocatalytic overall water splitting of CN180 with ~1.4 wt% Pt as the cocatalyst. Reprinted with permission from ref. 140, © Elsevier B.V. 2021. (c) Illustration of the formation process of O-doped g-C_3N_4 nanosheets (OCNs). (d) EEM fluorescence spectra of the residual RhB solution before reaction and after reaction for 2 min, 4 min and 6 min, respectively. Reprinted with permission from ref. 144, © Royal Society of Chemistry 2022. (e) Synthesis of g-C_3N_4 nanosheets through post-treatment and one-step exfoliation using ammonium salts. (f) Photocatalytic degradation of OTC with BCN and CNN-Br_x samples under visible-light irradiation. Reprinted with permission from ref. 145, © Elsevier B.V. 2019.

mass and charge transport *via* cross-plane diffusion channels. In addition, the protonation of g-C_3N_4 polymer enhanced charge separation and enlarged the specific surface area. The large specific surface area and micro/mesoporous structure of P–PCNNS resulted in higher CO_2 uptake ability (6.6 cm^3 g^{-1}) than that for bulk g-C_3N_4 (0.4 cm^3 g^{-1}) and ultrathin g-C_3N_4 nanosheets without protonation (2.5 cm^3 g^{-1}). The synergetic effects of the large specific surface area, low carrier recombination rate and strong CO_2 adsorption ability resulted in P–PCNNS with the highest CO_2-to-CO conversion rate ($\sim$1.23 μmol g^{-1} h^{-1}) under visible-light irradiation.

5. Polymer nanosheet-based heterostructures for photocatalysis

Although single-component polymer nanosheets have displayed conspicuous advantages in the field of photocatalysis, the rapid carrier recombination rate still seriously limits their photocatalytic activity, especially in the photocatalytic overall water splitting and CO_2 reduction. Recently, polymer nanosheet-based heterostructures are designed and prepared, which reveal remarkably elevated photocatalytic performance.

5.1 CMP nanosheet-based photocatalysts

5.1.1 Photocatalytic water splitting

5.1.1.1 Photocatalytic overall water splitting. Xu *et al.* synthesized ultrathin aza-CMP and C_2N nanosheets by the liquid-phase exfoliation method.[147] aza-CMP/C_2N van der Waals heterostructures were obtained *via* annealing the mixture of the two different nanosheets. Their electronic band structures resulted in the formation of Z-scheme photocatalytic systems, in which the aza-CMP and C_2N served as O_2- and H_2-evolving catalysts, respectively (Fig. 8a). The heterostructures facilitated photogenerated charge separation and transfer. When the mass ratio of aza-CMP and C_2N was 1 : 1, a high STH conversion efficiency (0.23%) was obtained. In contrast, the heterostructures formed from bulk aza-CMP and bulk C_2N did not exhibit overall water splitting activity, indicating that the ultrathin sheet-like structure of heterostructures were beneficial for charge utilization. In order to further enhance photocatalytic activity, reduced graphene oxide (RGO) sheets were used as good solid electron mediators to shuffle electrons from aza-CMP nanosheets to C_2N nanosheets (Fig. 8b). The photocatalytic overall water splitting rate under visible light irradiation (Fig. 8c) and STH conversion efficiency (0.40%) of the aza-CMP/RGO/C_2N heterojunction were nearly twice as much as those of aza-CMP/C_2N. When Pt and $Co(OH)_2$ cocatalysts were loaded onto C_2N and aza-CMP nanosheets, respectively, the STH conversion efficiency of the aza-CMP/RGO/C_2N heterojunction reached up to 0.73%, highlighting the potential of the ultrathin polymer nanosheets for achieving high overall water splitting activity.

5.2 COF nanosheet-based photocatalysts

5.2.1 Photocatalytic water splitting

5.2.1.1 Photocatalytic H_2 production. Zang *et al.* firstly used 2,3,6,7,10,11-hexaiminotriphenylene (HATP·6HCl), 2,6-diformylphenol (DFP) and $Cu(OAc)_2$ as raw materials to synthesize bulk binuclear Cu-salphen-HDCOF. And then, facile solvent-assisted liquid sonication was adopted to exfoliate it into Cu-salphen-HDCOF nanosheets with a thickness of around 2.4–3.6 nm (Fig. 8d and e),[148] in which the isolated Cu served as the active site. The synergistic effect of the π-conjugated framework of the COF and sufficient Cu active sites not only efficiently increased the access of photogenerated charges to the redox reaction centers on the surface of the photocatalyst, but also inhibited photocarrier recombination (Fig. 8f). In addition, the nanosheet morphology was beneficial for enhancing the number of exposed Cu active sites. Therefore, in the presence of the TEA sacrificial reagent and fluorescein photosensitizer, the Cu-salphen-HDCOF nanosheets exhibited an excellent H_2 evolution rate (36.99 mmol g^{-1} h^{-1}) under visible-light irradiation, which was much higher than that of bulk Cu-salphen-HDCOF and salphen-HDCOF nanosheets. Xi *et al.* employed β-ketoenamine-linked TpPa-1-COF nanosheets and g-C_3N_4 nanosheets to construct a π–π conjugated S-scheme heterojunction (Fig. 8g and h).[149] The formed built-in electric field enhanced charge separation and utilization. When the mass ratio of TpPa-1-COF nanosheets to g-C_3N_4 nanosheets was 2 : 1, the highest photocatalytic hydrogen evolution rate (1153 μmol g^{-1} h^{-1}) was obtained under visible-light irradiation, which was approximately 2.8 and 4.2 times as high as that for the TpPa-1-COF nanosheets and the g-C_3N_4 nanosheets, respectively. The TpPa-1-COF nanosheets were also employed by Shi *et al.* to construct a heterojunction with TiO_2 nanosheets *via* a solvothermal strategy.[150] Different from the above S-scheme heterojunction, the TpPa-1-COF nanosheets were used as the photosensitizer in the 2D/2D COF-TpPa-1/TiO_2 heterojunction. The photoinduced electrons were transferred from COF-TpPa-1 to TiO_2 under visible-light irradiation due to their different band edges. The intimate hetero-interface contact between them enhanced charge migration. Therefore, the COF-TpPa-1/TiO_2 heterojunction with a mass ratio of 14/6 achieved the highest hydrogen evolution rate (1.37 mmol g^{-1} h^{-1}) under visible-light irradiation, which was $\sim$29 times as high as that of COF-TpPa-1.

In addition, COF nanosheets also can serve as a special modifier to improve the photocatalytic H_2 yield rate of other semiconductors. For example, Yan *et al.* prepared a CNS–COF nanosheet heterojunction *via* the reaction of graphitic carbon nitride nanosheets (CNS) with 4,4′,4″-(1,3,5-triazine-2,4,6-triyl) trianiline (TTA) and 1,3,5-tri-formylphloroglucinol (TP). In the heterojunction, the percentage of COF nanosheets was below 2%.[151] The small amount of COF nanosheets integrated with the CNS through chemical imine bonding, which not only significantly passivated the surface termination of CNS, but also enhanced charge separation due to the strong electronic coupling between them. Under optimum conditions, the CNS–COF nanosheet heterojunction could achieve a H_2 yield rate of 46.4 mmol g^{-1} h^{-1} under visible-light irradiation, which was much better than that of the CNS itself.

5.2.2 Photocatalytic CO_2 reduction. Jiang *et al.* used an imine-exchange synthesis strategy for synthesizing a series of ultrathin imine-based 2D COF nanosheets with a thickness of

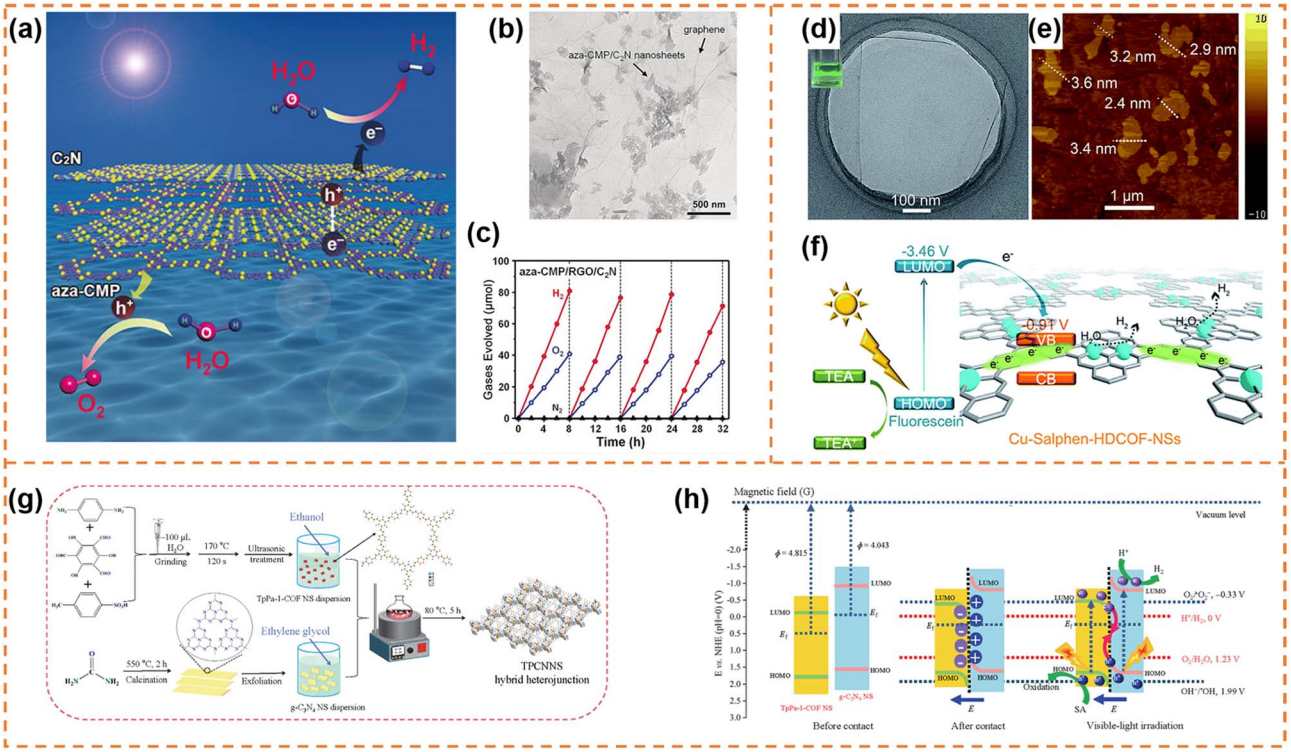

Fig. 8 (a) Illustration of the Z-scheme structure of aza-CMP and C_2N nanosheets. (b) TEM image of the aza-CMP/RGO/C_2N photocatalyst. (c) Typical time course of H_2 and O_2 production using the aza-CMP/RGO/C_2N photocatalyst under visible-light irradiation. Reprinted with permission from ref. 147, © Wiley-VCH GmbH 2018. (d) HR-TEM and (e) AFM images of Cu-salphen-HDCOF-NSs. (f) Schematic of the charge dynamics and hydrogen production mechanism of Cu-salphen-HDCOF-NSs. Reprinted with permission from ref. 148, © Royal Society of Chemistry 2020. (g) Preparation of the TpPa-1-COF/g-C_3N_4 NS (TPCNNS) hybrid heterojunction. (h) Schematic explanation of the charge migration mechanism in the S-scheme TPCNNS heterostructure before contact, after contact in darkness, and irradiated with visible light. Reprinted with permission from ref. 149, © Elsevier B.V. 2022.

less than 2.1 nm on a large scale and in high yield.[152] Among them, the COF-367-Co nanosheets with a thickness of about 1 nm (Fig. 9a) were prepared using CoTAPB and 2,4,6-trimethylbenzaldehyde (TBA) as the building blocks, possessing high adsorption capacity of CO_2 (34.4 $cm^3\ g^{-1}$) and abundant Co–N_4 active catalytic sites. The COF-367-Co nanosheets exhibited a high photocatalytic CO_2-to-CO conversion rate (10 162 μmol $h^{-1}\ g^{-1}$) and CO selectivity (*ca.* 78%) under visible-light irradiation ($\lambda \geq 420$ nm). Its CO_2-to-CO conversion rate was ~82 times that of bulk COF-367-Co, highlighting the significant advantage of COF nanosheets in photocatalytic CO_2 reduction. More importantly, the CO evolution rate and selectivity for COF-367-Co nanosheets showed almost no decline after six successive cycles (Fig. 9b). Different from one step synthesis of a Co-containing COF by Jiang *et al.*, Copper *et al.* firstly synthesized FPy-COF *via* a Schiff base condensation reaction, and then ultrasonicated it in acetonitrile containing $CoCl_2$ to obtain Co-loaded COF nanosheets (denoted as Co-FPy-CON).[153] Co-FPy-CON had a thickness of 1.9–4.4 nm and a BET surface area of 238 $m^2\ g^{-1}$. Its fluorinated moieties could polarize CO_2, resulting in high CO_2 adsorption ability. However, it exhibited very low CO_2 reduction activity in the presence of a hole scavenger. When the (Ir[dF(CF$_3$)-ppy]$_2$(dtbpy))PF6 dye was used as the photosensitizer (Fig. 9c), the new system worked efficiently, which could produce 10.1 μmol CO over 6 h with a selectivity of 76% under visible-light irradiation (Fig. 9d). The reason was that Co-FPy-CON served as a semiconductor support (transferring charge carriers generated in the dye to the Co centers) rather than as a photocatalyst itself. Its excellent selectivity, durability and cyclability were comparable to those of the most advanced visible-light driven polymers.

5.3 CTF nanosheet-based photocatalysts

5.3.1 Photocatalytic water splitting

5.3.1.1 Photocatalytic H_2 production. Zou *et al.* firstly prepared benzoic acid-functionalized CTF-1 nanosheets (denoted as B-CTF-1) by the chemical grafting modification method, and then constructed a type II heterojunction with amino-functionalized Ti-based NH_2-MIL-125(Ti) using a step-by-step post-synthetic covalent modification method (Fig. 9e).[154] The two components were tightly bound through amide bonds. More importantly, the photogenerated electrons were transferred from the CB of NH_2-MIL-125(Ti) to the CB of B-CTF-1 through the amide bridge bonds. Therefore, the amide bonds as a charge transfer mediator promoted photogenerated carrier separation and improved the stability of the photocatalyst (Fig. 9f). Under optimum conditions, the formed heterojunction exhibited a H_2 production rate of 360 μmol $h^{-1}\ g^{-1}$ under

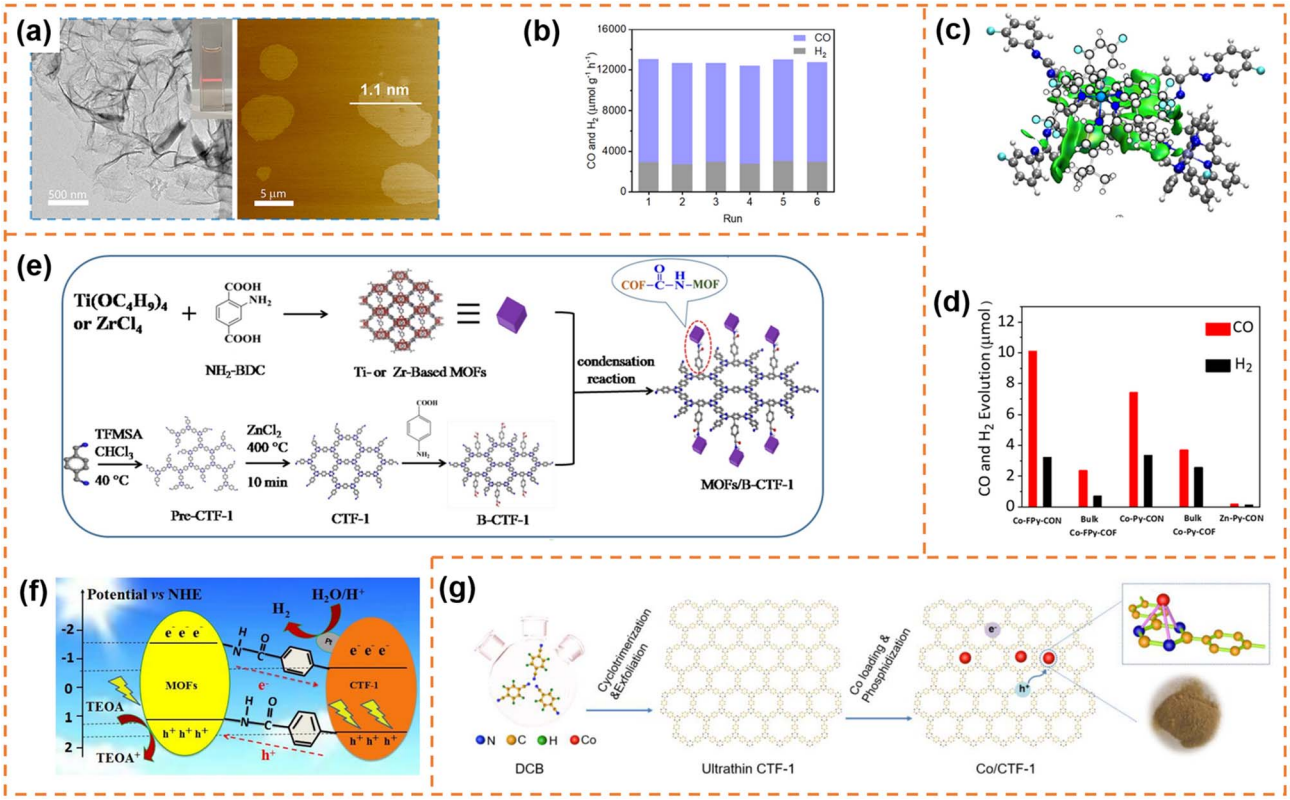

Fig. 9 (a)TEM and AFM images of the as-prepared COF-367-Co NSs. (b) Stability tests of COF-367-Co NSs for the photocatalytic reduction of CO_2. Reprinted with permission from ref. 152, © American Chemical Society 2019. (c) DFT-optimized adsorption configuration of the dye on the pyrene moiety of Co-FPy-COF. (d) CO and H_2 production by the nanosheet and bulk Co-FPy-COF, Co-Py-COF, and Co-Bp-COF, over 6 h under visible light irradiation. Reprinted with permission from ref. 153, © American Chemical Society 2020. (e) Schematic illustration of the formation of the TBC hybrid material. (f) Photocatalytic mechanism of the charge transfer for hydrogen evolution over 15TBC under visible light irradiation. Reprinted with permission from ref. 154, © Elsevier B.V. 2019. (g) Schematic illustration of the preparation process of Co/CTF-1. Reprinted with permission from ref. 155, © Elsevier B.V. 2022.

visible-light irradiation, which was more than twice as high as that of B-CTF-1.

5.3.2 Photocatalytic degradation. Liu *et al.* firstly prepared ultrathin CTF-1 nanosheets by ultrasonic exfoliation, and then used $Co(NO_3)_2$ as the raw material to load single-atom Co on the nanosheets *via* pyrolysis and phosphorization (denoted as Co/CTF-1) (Fig. 9g).[155] Co atoms were uniformly dispersed onto ultrathin CTF-1, and the two components were tightly bound through a stable Co–N_3 architecture. The Co single atoms in the CTF-1 skeleton served as oxidation centers to capture holes from ultrathin CTF-1, which could enhance charge separation. Therefore, in the presence of H_2O_2, Co/CTF-1 exhibited excellent MB photodegradation efficiency (99.9%) under visible-light irradiation, which was much better than that of pristine CTF-1 (68.8%). In the photodegradation process, holes and superoxide radicals were dominant active species.

5.3.3 Photocatalytic CO_2 reduction. Bai *et al.* firstly obtained CTF nanosheets (denoted as CTFN) using an ultrasonication-assisted exfoliation method, and then loaded ultrafine Ag nanoparticles on them *via* a solution infiltration method (denoted as Ag^0@CTFN) (Fig. 10a).[156] Ag nanoparticles were encapsulated in the CTFN interlayers through the interaction between N sites of triazine units and Ag nanoparticles. Compared with the CTF, Ag^0@CTFN exhibited high photocatalytic activity and good recyclability in the carboxylation of various alkynes with CO_2 under mild conditions. In the CO_2 transformation process (Fig. 10b), the Ag nanoparticles coordinated terminal alkynes with Cs_2CO_3 to form a silver acetylide intermediate. Meanwhile, CO_2 was adsorbed on the basic sites of the CTFN and activated into electrophilic species, which subsequently could attack the silver acetylide to form the silver carboxylate. In the presence of Cs_2CO_3 and alkynes, the silver carboxylates were quickly transferred to cesium carboxylate through transmetallation, and the cesium carboxylate could be acidified to generate carboxylic acid products. More importantly, their photocatalytic performance did not exhibit a significant loss after six recycles (Fig. 10c).

The self-assembly method was also a commonly used method to prepare CTF nanosheet-based heterojunctions for CO_2 photoreduction.[157,158] For example, Zhong *et al.* synthesized black phosphorus (BP)/CTF nanosheets (denoted as CTF-BP) with a thickness of ~1.2 nm.[157] The strong interaction between CTF and BP resulted in fast charge transfer, and the CO production rate of CTF-BP under visible-light irradiation was 3 and 2 times higher than that of BP and CTF, respectively. More importantly, the strong interaction between CO and CTF-BP could prevent CO

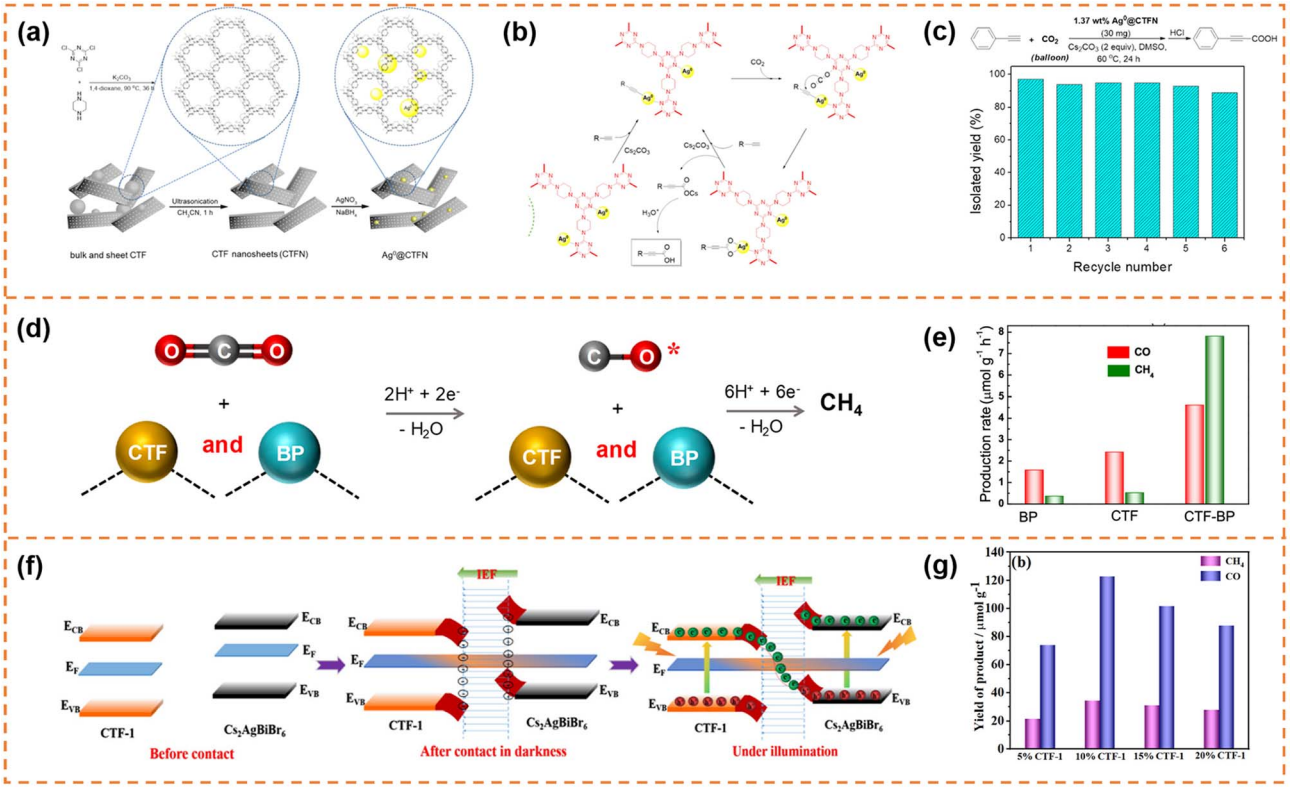

Fig. 10 (a) Illustration of the design and preparation procedure of Ag^0@CTFN nanocomposites. (b) A proposed mechanism for the carboxylation of terminal alkynes with CO_2. (c) Reuse of the Ag^0@CTFN catalyst. Reprinted with permission from ref. 156, © American Chemical Society 2018. (d) Photocatalytic reaction mechanism over the CTF-BP heterostructured catalyst. (e) Averaged production rates of CO and CH_4. Reprinted with permission from ref. 157, © American Chemical Society 2020. (f) Schematic illustration of the S-scheme charge transfer mechanism between CTF-1 NSs and $Cs_2AgBiBr_6$ NSs. (g) CO_2 photoreduction performance of the CABB/CTF-1 hybrids with different contents of CTF-1 after 4 h of visible illumination. Reprinted with permission from ref. 158, © American Chemical Society 2022.

desorption from the photocatalyst surface, which was beneficial for photoreducing CO_2 to CH_4 *via* an 8-electron process (Fig. 10d). Therefore, the CTF-BP catalyst exhibited a high CH_4 production rate of 7.81 μmol g^{-1} h^{-1} under visible-light irradiation, which was 23 and 16 times higher than that of BP and CTF, respectively (Fig. 10e). Xu *et al.* prepared $Cs_2AgBiBr_6$ nanosheets and CTF-1 nanosheets.[158] The ionization of surface capping ligands resulted in $Cs_2AgBiBr_6$ with positive charges, and the lone pair electrons of the nitrogen atoms in the triazine units resulted in CTF-1 with negative charges, so the $Cs_2AgBiBr_6$/CTF-1 (denoted as CABB/CTF-1) nanosheet heterojunction with a large surface-to-surface contact could be formed through electrostatic self-assembly. The two components formed an S-scheme heterojunction, resulting in efficient electron transfer and high redox capacity (Fig. 10f). The CABB/CTF-1 heterojunction with 10% CTF-1 (Fig. 10g) exhibited the highest photocatalytic CO_2 reduction activity under visible-light irradiation (~30.7 μmol g^{-1} h^{-1} for CO and 8.6 μmol g^{-1} h^{-1} for CH_4), which was much better than that of the $Cs_2AgBiBr_6$ nanosheets and CTF-1 nanosheets.

5.4 Carbon nitride nanosheet-based photocatalysts

Carbon nitride nanosheet-based heterojunctions have been widely reported. In this section, heterojunctions formed from exfoliated carbon nitride nanosheets with other zero-dimensional (0D)/one-dimensional (1D)/2D/three-dimensional (3D) photocatalysts are briefly displayed and their photocatalytic performances are discussed.

5.4.1 Photocatalytic water splitting

5.4.1.1 Photocatalytic H_2 production. Li *et al.* inserted 0D N-doped carbon dots (NCDs) onto g-C_3N_4 nanosheets with a thickness of 1 nm *via* a two-step thermal exfoliation method.[159] The introduction of NCDs provided catalytic active sites and shortened the distance of charge transfer to the g-C_3N_4 surface. Compared with bulk g-C_3N_4/NCDs, g-C_3N_4 nanosheet/NCDs possessed a larger number of exposed NCDs, and thus exhibited a better photocatalytic H_2 production rate. Under optimal conditions, its H_2 production rate reached 3319.3 μmol g^{-1} h^{-1}, which was about 13 fold that of bulk g-C_3N_4 and 2.7 fold that of bulk g-C_3N_4/NCDs. Jia *et al.* prepared an isotype heterojunction of 1D/2D g-C_3N_4 through thermal polymerization (melamine grafted with ethylenediamine was used as the precursor) and subsequent HCl-assisted hydrothermal exfoliation (Fig. 11a).[160] In the preparation process, the grafted ethylenediamine limited the directional growth of g-C_3N_4 into nanowires and introduced carbon doping, and the exfoliation resulted in ultrathin g-C_3N_4 nanosheets. The carbon doping increased visible-light absorption ability. And the ultra-thin nanosheets provided more photogenerated charges to

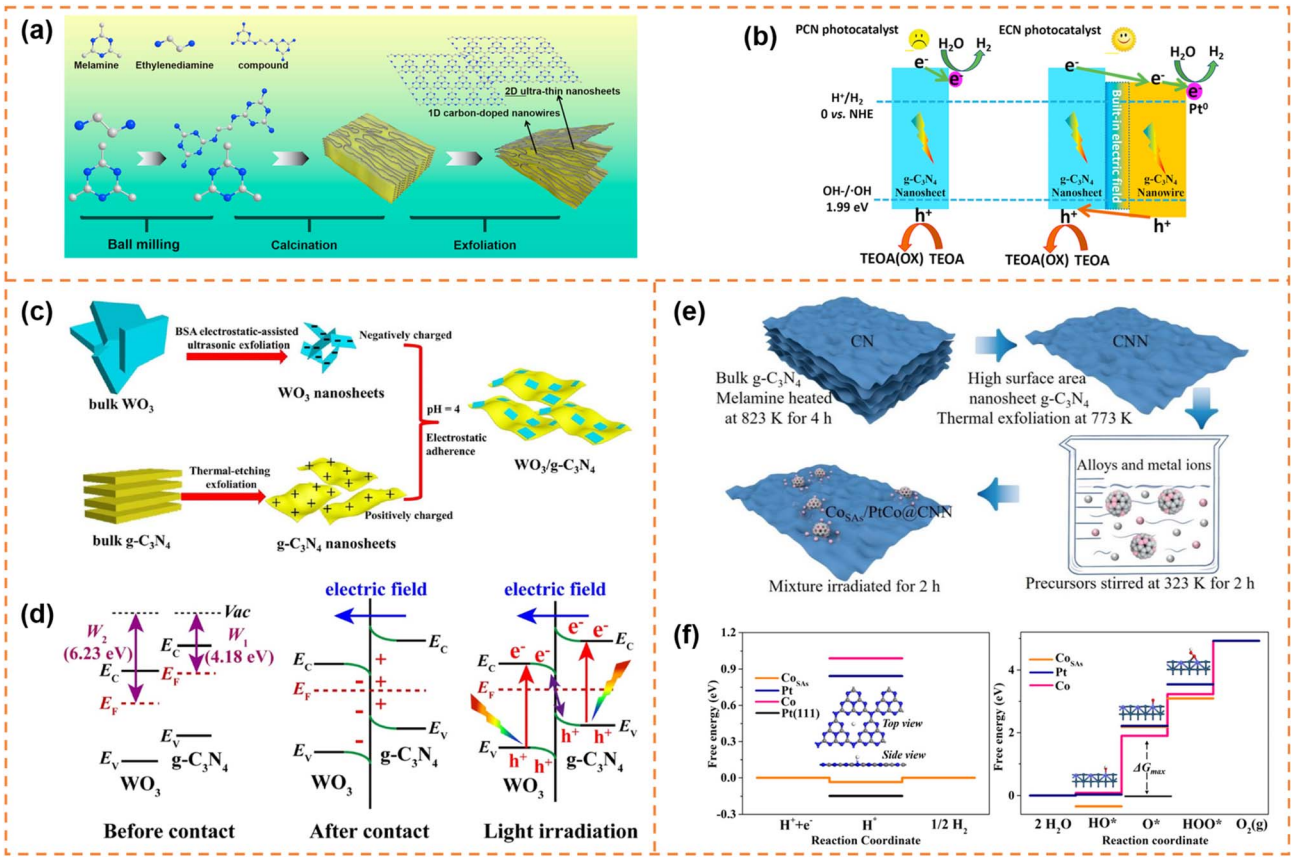

Fig. 11 (a) Schematic representation of the preparation process of U-ECN. (b) The migration direction of photogenerated electrons and holes and the possible mechanism of PCN and ECN for photocatalytic H_2 evolution. Reprinted with permission from ref. 160, © Elsevier B.V. 2021. (c) The formation schematic diagram of 2D/2D WO_3/g-C_3N_4 heterojunctions by coulomb electrostatic interaction. (d) The S-scheme formation mechanism between WO_3 and g-C_3N_4. Reprinted with permission from ref. 161, © Elsevier B.V. 2019. (e) Schematic illustration of the synthetic strategy of producing the CoSAs/PtCo@CNN sample. (f) Free energy diagram for the HER and the OER under standard conditions for the CoSAs/PtCo@CNN catalyst. Reprinted with permission from ref. 163, © American Chemical Society 2022.

participate in the transfer among isotype heterojunctions. Moreover, the formed built-in electric field between the two components facilitated rapid migration of photogenerated charges at the interface (Fig. 11b). Therefore the photocatalytic H_2 evolution activity of the isotype heterojunction under visible-light irradiation was 8.2 times that of pristine g-C_3N_4. Yu *et al.* fabricated ultrathin WO_3 and g-C_3N_4 nanosheets with a thickness of 2.5–3.5 nm by electrostatic-assisted ultrasonication of bulk WO_3 and thermal-etching exfoliation of bulk g-C_3N_4, respectively (Fig. 11c).[161] The ultrathin WO_3/g-C_3N_4 nanosheets formed an S-scheme heterojunction through electrostatic self-assembly (Fig. 11d). The ultrathin layered heterojunction structure was beneficial for the transfer of photogenerated electrons and holes at the heterogeneous interface to the surface of photocatalysts, and the S-scheme heterojunction inhibited the recombination of useful electrons and holes. Therefore the H_2-production activity of the WO_3/g-C_3N_4 nanosheets under xenon lamp irradiation was better than that of pure g-C_3N_4 and WO_3 nanosheets. Parida *et al.* deposited $MgIn_2S_4$ microflowers onto the surface of exfoliated B-doped g-C_3N_4 nanosheets (e-BCN) to form a p–n heterojunction.[162] e-BCN provided abundant active sites to the $MgIn_2S_4$ microflowers for water molecule adsorption, and the built-in electric field inhibited carrier recombination. Under the optimal conditions, the heterojunction exhibited an excellent photocatalytic H_2 generation rate with an apparent conversion efficiency of 5.27%.

5.4.1.2 Photocatalytic overall water splitting. Yao *et al.* anchored 0D single-atom Co and PtCo alloy nanoparticles on exfoliated g-C_3N_4 nanosheets to achieve overall water splitting (Fig. 11e).[163] The single-atom Co and PtCo alloys acted as highly active sites for the hydrogen evolution reaction and the oxygen evolution reaction, respectively (Fig. 11f). In addition, the authors suggested that there might be a spillover phenomenon of protons or hydroxyl groups between the single-atom Co centers and PtCo alloy nanoparticles. Ajayan *et al.* used small amounts of α-Fe_2O_3 nanosheets to promote exfoliation of g-C_3N_4.[164] Meanwhile, the α-Fe_2O_3 nanosheets and g-C_3N_4 nanosheets were tightly bound and formed an all-solid-state Z-scheme heterojunction, which served as an oxidation counterpart and reduction counterpart, respectively. Thanks to the Z-scheme structure and tight interface, electron–hole recombination in both materials was effectively inhibited, which resulted in good overall water splitting activity under visible-light irradiation.

5.4.2 Photocatalytic degradation. Yang *et al.* firstly prepared g-C_3N_4 nanosheets (CNNSs) and 0D SnO_2 nanoparticles (NPs) *via* multiple thermal exfoliation and hydrothermal methods, respectively.[165] And then the electrostatic self-assembly method was used to construct a SnO_2 nanoparticles/g-C_3N_4 nanosheet type II heterojunction. The built-in electric field could specify the charge transfer direction and promote charge separation. In addition, the re-adjustment of the band created new energy level platforms in SnO_2 and CNNSs, improving the redox capacity of the heterojunction. Therefore the heterojunction exhibited an excellent RhB degradation activity (96.9% within 50 min) under visible-light irradiation. Li *et al.* used a simple hydrothermal method and *in situ* calcination to obtain ZnO nanorods/K-doped exfoliated g-C_3N_4 nanosheet type-II heterojunctions (Fig. 12a).[166] The excellent interface contact and strong interaction between the two components promoted the absorption of sunlight as well as separation and migration of photogenerated carriers (Fig. 12b). In addition, the changed surface ζ-potential enhanced the adsorption capacity to tetracycline. Therefore the synergistic effects of photocatalysis and adsorption enabled the optimized type-II heterojunction to achieve a tetracycline degradation rate of 90% under simulated sunlight irradiation. Basu *et al.* covered BiOCl nanoplates on g-C_3N_4 nanosheets *via* a hydrothermal method.[167] The formed heterojunction had a high surface-area, narrow bandgap and low recombination rate, which exhibited good degradation performance of color (methylene blue)/colorless (imidacloprid) pollutants under natural sunlight irradiation. Zhu *et al.* coated

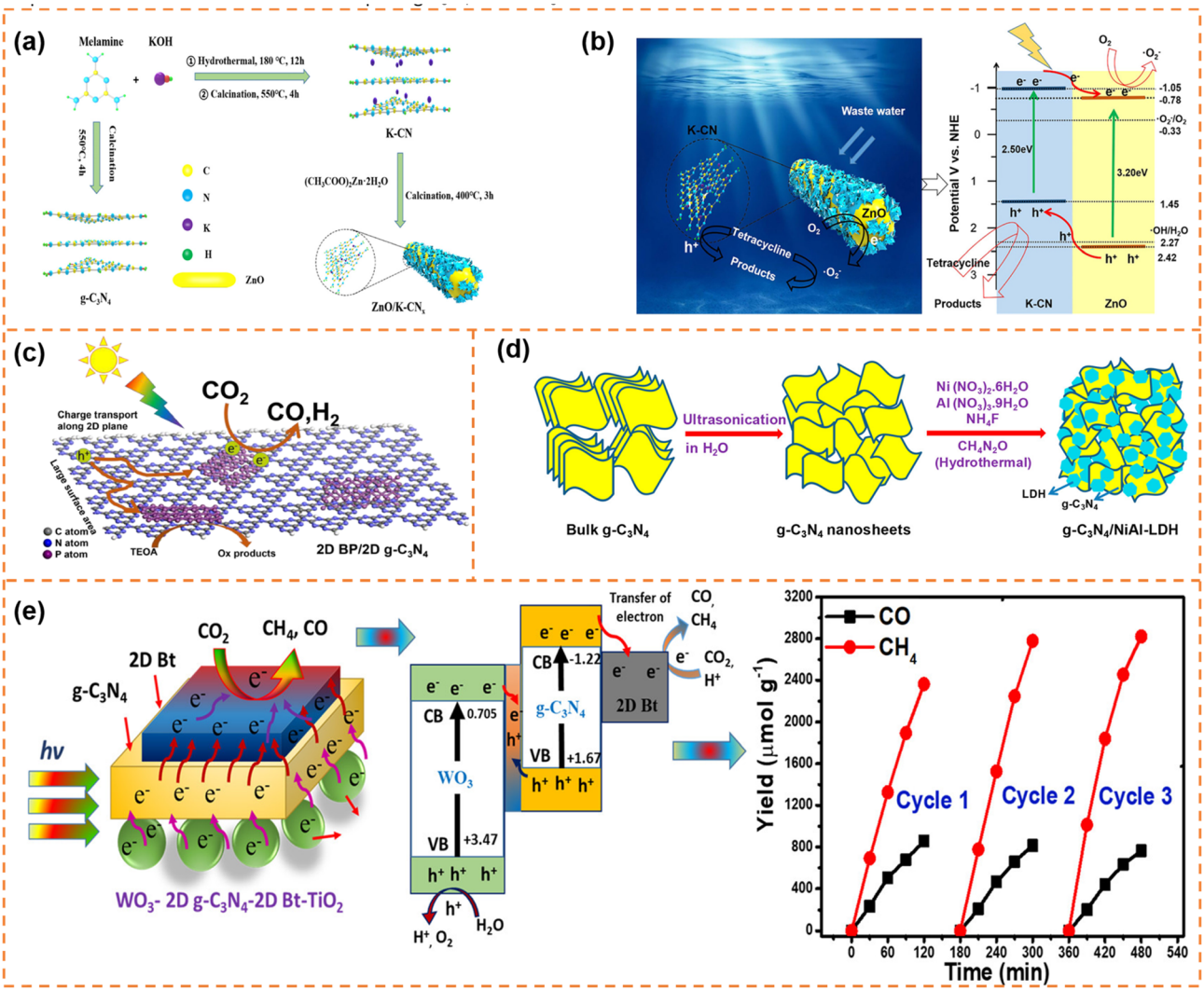

Fig. 12 (a) Schematic diagram of the synthesis and assembly route of photocatalyst materials. (b) Schematic diagram of the charge separation and photocatalytic mechanism of type-II ZnO/K-CN0.5 heterojunctions under simulated sunlight. Reprinted with permission from ref. 166, © American Chemical Society 2020. (c) Illustration of the photocatalytic mechanism of the 2D BP/2D g-C_3N_4 system under visible-light irradiation. Reprinted with permission from ref. 169, © Elsevier B.V. 2020. (d) Schematic illustration of the synthesis process of g-C_3N_4/NiAl-LDH hybrid heterojunctions. Reprinted with permission from ref. 170, © American Chemical Society 2018. (e) Proposed mechanism and stability analysis of photocatalytic CO_2 reduction with H_2O over the Bt-mediated WO_3/g-C_3N_4 composite under visible-light irradiation. Reprinted with permission from ref. 172, © American Chemical Society 2020.

g-C_3N_4 nanosheets (CN) or Eu doped g-C_3N_4 nanosheets (Eu-CN) on the surface of flower-like $BiVO_4$ through sonication impregnation and heating processes, forming a core–shell heterojunction (CN@$BiVO_4$ or Eu-CN@$BiVO_4$).[168] The tight contact between the two components was beneficial for charge transfer across the interface, and therefore the tetracycline degradation performance of CN@$BiVO_4$ was better than that of $BiVO_4$. In addition, the degradation rate of Eu-CN@$BiVO_4$ was higher than that of CN@$BiVO_4$ because the Eu(III) in Eu-CN@$BiVO_4$ could capture photoinduced electrons and enhance the photogenerated carrier migration and separation rate.

5.4.3 Photocatalytic CO_2 reduction. The large specific surface area is conducive to CO_2 adsorption, so most reported g-C_3N_4 nanosheet based heterojunctions are 2D/2D and 2D/3D heterojunctions. For example, Li *et al.* used freezing exfoliation and thermal exfoliation methods to prepare ultrathin black phosphorus (BP) and g-C_3N_4 nanosheets, respectively, and then obtained a 2D BP/2D g-C_3N_4 heterostructure by freeze-drying treatment.[169] The tight contact extremely boosted the separation of photogenerated carriers (Fig. 12c), resulting in an excellent CO generation rate (187.7 μmol g^{-1} h^{-1}) and high selectivity for CO (92.55%). Ogale *et al.* prepared 2D/2D interface heterostructures of g-C_3N_4 and NiAl-LDH nanosheets *via* electrostatic self-assembly (Fig. 12d).[170] The synergistic effect of a strong interfacial contact and effective separation and transfer of photogenerated carriers resulted in an enhanced CO production rate. Yu *et al.* constructed a 2D/3D g-C_3N_4/ZnO S-scheme heterojunction.[171] The ZnO hollow spheres were wrapped by 2D g-C_3N_4 layers, and the electrostatic attraction between them facilitated the exfoliation of g-C_3N_4 layers and strengthened the photocatalyst framework. The extended light absorption and suppressed charge carrier recombination resulted in a high CH_4 production rate of the heterojunction, which was about 40 and 7 times higher than that of pure ZnO and g-C_3N_4, respectively. Tahir *et al.* designed a 3D/2D/2D WO_3/bentonite/g-C_3N_4 Z-scheme heterojunction through a facile ultrasonication approach.[172] WO_3-coupled with g-C_3N_4 was favorable for CO production. In contrast, the Z-scheme of the WO_3/g-C_3N_4 composite with bentonite as the electron moderator was in favor of CH_4 formation during the CO_2 reduction process, which led to a high quantum yield of 20.106% and an excellent selectivity of 72.82% for CH_4 (Fig. 12e).

6. Conclusions and prospects

We summarized the recent advances in polymer (CMPs, COFs, CTFs and carbon nitrides) nanosheets for photocatalysis, including water splitting, pollutant degradation and CO_2 reduction. Besides the conventional advantages of low cost, good visible-light absorption ability and chemical stability, as well as tunable electronic and optical properties, polymer nanosheets have some special virtues, such as a short carrier migration distance, atomic-level regulation of the backbone and targeted introduction of active sites. Therefore polymer nanosheets generally exhibit better photocatalytic activity than bulk polymers and most traditional inorganic semiconductors. In addition, the abundant surface active groups and conjugated porous architecture of polymer nanosheets provide the potential for tightly bonding with organic or inorganic materials to form heterojunctions.

Although significant progress has been achieved in these photocatalytic applications, polymer nanosheets and their heterojunctions still face some obvious challenges. (1) The preparation methods of polymer nanosheets have rarely been reported, especially for single-layer/few-layer nanosheets. Meanwhile, the large-scale preparation of polymer nanosheets is also highly challenging. (2) The structural properties of polymer nanosheets like thickness, size and surface active groups have great effects on photocatalytic performance, yet there are few in-depth reports. (3) The effective guidance for obtaining high-performance polymer nanosheets is still lacking. Effective theoretical prediction of structural properties (such as surface active sites and backbone) is encouraged, which can avoid many useless experimental studies. For example, Cooper *et al.* integrated robotic experimentation with high-throughput computation and discovered new polymers with high H_2 production activity.[173] (4) Polymer nanosheet-based heterojunctions for photocatalytic application are still rarely reported, especially those formed by *in situ* growth. Compared with the common self-assembly method, the bonds formed by *in situ* growth are more stable, which benefit charge transfer and photostability. (5) Due to the poor water oxidation ability caused by slow surface dynamics,[174] it is still difficult for polymer nanosheets to achieve overall water splitting. Many inorganic semiconductors with good visible-light absorption ability possess excellent water oxidation ability, so it is very valuable to construct S-scheme or Z-scheme heterojunctions between polymer nanosheets and these inorganic semiconductors. (6) The photocatalytic CO_2 reduction activity of polymer nanosheets and their heterojunctions is still low, especially for reducing CO_2 to high-value chemicals (CH_4 *etc.*). In addition, the reductive half reaction of the CO_2 transformation process has been densely reported, while the oxidation half reaction (H_2O oxidation, *etc.*) is rare. (7) The photodegradation of polymer nanosheets and their heterojunctions mainly focuses on dye degradation. It can be extended to more types of pollutants (such as antibiotics and volatile organic compounds) to further improve their practicability.

Despite these challenges, the inherent advantages of polymer nanosheets and their heterojunctions bring about infinite opportunities to achieve high photocatalytic activity. We expect that this review can provide a helpful reference for the rapid development of polymer nanosheets for photocatalysis.

Conflicts of interest

There are no conflicts to declare.

Acknowledgements

This work was supported by the National Natural Science Foundation of China (No. 22022510, 51872186, and 22066024).

References

1 A. J. Carrillo, J. González-Aguilar, M. Romero and J. M. Coronado, *Chem. Rev.*, 2019, **119**, 4777–4816.
2 N. S. Lewis and D. G. Nocera, *Proc. Natl. Acad. Sci. U. S. A.*, 2006, **103**, 15729–15735.
3 Y. Du, Y. Wang, J. Wu, Q. Chen, C. Deng, R. Ji, L. Sun, L. Tan, X. Chen and Y. Xie, *InfoMat*, 2023, e12431.
4 Y. Lin, H. Kuang, S. Zhang, X. Zhang, G. Zhai, X. Lin, D. Xu, J. Jia, X. Li and J. Chen, *CCS Chem.*, 2022, **4**, 3482–3490.
5 H. Li, C. Chen, H. Hu, Y. Li, Z. Shen, F. Li, Y. Liu, R. Liu, J. Chen and C. Dong, *InfoMat*, 2022, **4**, e12322.
6 Y. Jiang, Y. Fan, S. Li and Z. Tang, *CCS Chem.*, 2023, **5**, 30–54.
7 C. H. Dai and B. Liu, *Energy Environ. Sci.*, 2020, **13**, 24–52.
8 Z. Gao, Y. Jian, S. Yang, Q. Xie, C. J. Ross Mcfadzean, B. Wei, J. Tang, J. Yuan, C. Pan and G. Yu, *Angew. Chem., Int. Ed.*, 2023, **62**, e202304173.
9 Q. Zuo, R. Cui, L. Wang, Y. Wang, C. Yu, L. Wu, Y. Mai and Y. Zhou, *Sci. China Chem.*, 2023, **66**, 570–577.
10 Q. Zuo, K. Feng, J. Zhong, Y. Mai and Y. Zhou, *CCS Chem.*, 2021, **3**, 1963–1971.
11 J. Liu, Y. Guo, Z. Hu, H. Zhao, Z. Yu, L. Chen, Y. Li, G. V. Tendeloo and B. Su, *CCS Chem.*, 2022, **5**, 372–384.
12 Z. Meng, Z. Qiu, Y. Shi, S. Wang, G. Zhang, Y. Pi and H. Pang, *eScience*, 2023, 100092.
13 A. Li, P. Zhang, E. Kan and J. Gong, *eScience*, 2023, 100157.
14 S. Wei, S. Chang, J. Qian and X. Xu, *Small*, 2021, **17**, 2100084.
15 Y. Bai, K. Hippalgaonkar and R. S. Sprick, *J. Mater. Chem. A*, 2021, **9**, 16222–16232.
16 X. Li, J. G. Yu, J. X. Low, Y. P. Fang, J. Xiao and X. B. Chen, *J. Mater. Chem.*, 2015, **3**, 2485–2534.
17 J. Wei, D. Luo, M. Shi, Q. Yuan, M. Wang, Y. Huang and Y. Ni, *Inorg. Chem.*, 2023, **62**, 10973–10983.
18 Q. Zuo, T. Liu, C. Chen, Y. Ji, X. Gong, Y. Mai and Y. Zhou, *Angew. Chem., Int. Ed.*, 2019, **58**, 10198–10203.
19 G. Zhang, X. Li, M. Wang, X. Li, Y. Wang, S. Huang, D. Chen, N. Li, Q. Xu, H. Li and J. Lu, *Nano Res.*, 2023, **16**, 6134–6141.
20 D. Zhao, Y. Wang, C. Dong, F. Meng, Y. Huang, Q. Zhang, L. Gu, L. Liu and S. Shen, *Nano-Micro Lett.*, 2022, **14**, 223.
21 K. M. Kamal, R. Narayan, N. Chandran, S. Popovic, M. A. Nazrulla, J. Kovac, N. Vrtovec, M. Bele, N. Hodnik, M. M. Krzmanc and B. Likozar, *Appl. Catal., B*, 2022, **307**, 121181.
22 F. L. Wang, R. Q. Fang, X. Zhao, X. P. Kong, T. T. Hou, K. Shen and Y. W. Li, *ACS Nano*, 2022, **16**, 4517–4527.
23 K. Li, B. S. Peng and T. Y. Peng, *ACS Catal.*, 2016, **6**, 7485–7527.
24 W. Pan, Z. Wei, Y. Su, Y. Lian, Z. Zheng, H. Yuan, Y. Qin, X. Xie, Q. Bai, Z. Jiao, W. Hua, J. Chen, W. Yang, Z. Deng and Y. Peng, *Nano Res.*, 2023, DOI: 10.1007/s12274-023-6083-2.
25 C. Ban, Y. Duan, Y. Wang, J. Ma, K. Wang, J. Meng, X. Liu, C. Wang, X. Han, G. Cao, L. Gan and X. Zhou, *Nano-Micro Lett.*, 2022, **14**, 74.
26 A. Ahmad, M. Ali, A. G. Al-Sehemi, A. A. Al-Ghamdi, J.-W. Park, H. Algarni and H. Anwer, *Chem. Eng. J.*, 2023, **452**, 139436.
27 S. Wei, S. Fan, M. Zhang, J. Ren, B. Jia, Y. Wang, R. Wu, Z. Fang and Q. Liang, *Mater. Today Sustainability*, 2023, **21**, 100311.
28 S. Wei, Y. Chen, P. Wu, X. Liu, J. Ren, B. Yao, H. Xu, W. Dou, Y. Wang and R. Wu, *Appl. Catal., A*, 2022, **640**, 118675.
29 F. He, X. Liu, X. Zhao, J. Zhang, P. Dong, Y. Zhang, C. Zhao, H. Sun, X. Duan and S. Wang, *J. Mater. Chem. A*, 2022, **10**, 20559–20570.
30 J. Luo, Z. Dai, M. Feng, M. Gu and Y. Xie, *Nano Res.*, 2023, **16**, 371–376.
31 X. Sun, L. Li, S. Jin, W. Shao, H. Wang, X. Zhang and Y. Xie, *eScience*, 2023, **3**, 100095.
32 A. Fujishima and K. Honda, *Nature*, 1972, **238**, 37–38.
33 J. Shi, G. Liu, N. Wang and C. Li, *J. Mater. Chem.*, 2012, **22**, 18808–18813.
34 W. Yu, J. Zhang and T. Peng, *Appl. Catal., B*, 2016, **181**, 220–227.
35 H. Tan, Z. Zhao, W.-b. Zhu, E. N. Coker, B. Li, M. Zheng, W. Yu, H. Fan and Z. Sun, *ACS Appl. Mater. Interfaces*, 2014, **6**, 19184–19190.
36 H. Xu, Y. Wang, X. Dong, N. Zheng, H. Ma and X. Zhang, *Appl. Catal., B*, 2019, **257**, 117932.
37 H. Jing, H. Li, J. Yue, S. Fan, B. Yao, S. Liu, Z. Fang, R. Wu, L. Yang and S. Wei, *Dalton Trans.*, 2023, **52**, 2924–2927.
38 H. Jing, J. Ren, J. Yue, S. Liu, Q. Liang, R. Wu, Y. Wang, Z. Fang, H. Li and S. Wei, *Catal. Sci. Technol.*, 2023, **13**, 226–232.
39 G. Lin, C. Zhang and X. Xu, *J. Mater. Sci. Technol.*, 2023, **154**, 241–250.
40 F. Zhang, A. Yamakata, K. Maeda, Y. Moriya, T. Takata, J. Kubota, K. Teshima, S. Oishi and K. Domen, *J. Am. Chem. Soc.*, 2012, **134**, 8348–8351.
41 S. Wei, S. Chang, F. Yang, Z. Fu, G. Liu and X. Xu, *Chem. Commun.*, 2021, **57**, 4412–4415.
42 L. Wang, Y. Zhang, L. Chen, H. Xu and Y. Xiong, *Adv. Mater.*, 2018, **30**, 1801955.
43 G. Zhang, Z. A. Lan and X. Wang, *Angew. Chem., Int. Ed.*, 2016, **55**, 15712–15727.
44 R. S. Sprick, J.-X. Jiang, B. Bonillo, S. Ren, T. Ratvijitvech, P. Guiglion, M. A. Zwijnenburg, D. J. Adams and A. I. Cooper, *J. Am. Chem. Soc.*, 2015, **137**, 3265–3270.
45 S. Yanagida, A. Kabumoto, K. Mizumoto, C. Pac and K. Yoshino, *J. Chem. Soc., Chem. Commun.*, 1985, 474–475.
46 Y. Jing, X. Zhu, S. Maier and T. Heine, *Trends Chem.*, 2022, **4**, 792–806.
47 J. M. Valero, S. Obregón and G. Colon, *ACS Catal.*, 2014, **4**, 3320–3329.
48 P. Chen, P. Xing, Z. Chen, H. Lin and Y. He, *Int. J. Hydrogen Energy*, 2018, **43**, 19984–19989.
49 Y. Bao, S. Song, G. Yao and S. Jiang, *Sol. RRL*, 2021, **5**, 2100118.
50 M. Dai, Z. He, P. Zhang, X. Li and S. Wang, *J. Mater. Sci. Technol.*, 2022, **122**, 231–242.

51 M. Gao, F. Tian, X. Zhang, Z. Chen, W. Yang and Y. Yu, *Nano-Micro Lett.*, 2023, **15**, 129.
52 S. F. Ng, J. J. Foo and W. J. Ong, *InfoMat*, 2022, **4**, e12279.
53 Q. Zhu, Z. Xu, B. Qiu, M. Xing and J. Zhang, *Small*, 2021, **17**, 2101070.
54 B. He, C. Bie, X. Fei, B. Cheng, J. Yu, W. Ho, A. A. Al-Ghamdi and S. Wageh, *Appl. Catal., B*, 2021, **288**, 119994.
55 H. Abdullah, M. M. R. Khan, H. R. Ong and Z. Yaakob, *J. CO_2 Util.*, 2017, **22**, 15–32.
56 D. Li, M. Kassymova, X. Cai, S. Zang and H. Jiang, *Coordin. Chem. Rev.*, 2020, **412**, 213262.
57 D. P. Tran, M. Pham, X. Bui, Y. Wang and S. You, *Sol. Energy*, 2022, **240**, 443–466.
58 V. Nguyen, B. Nguyen, Z. Jin, M. Shokouhimehr, H. W. Jang, C. Hu, P. Singh, P. Raizada, W. Peng and S. S. Lam, *Chem. Eng. J.*, 2020, **402**, 126184.
59 J. Ran, M. Jaroniec and S. Z. Qiao, *Adv. Mater.*, 2018, **30**, 1704649.
60 P. M. Wood, *Biochem. J.*, 1988, **253**, 287.
61 X. Du, T. Zhao, Z. Xiu, Z. Xing, Z. Li, K. Pan, S. Yang and W. Zhou, *Appl. Mater. Today*, 2020, **20**, 100719.
62 X. Zhang, L. Jian, L. Wang, R. Liu, Y. Zhao, Y. Li and C. Wang, *Appl. Surf. Sci.*, 2022, **571**, 151304.
63 S. Yang, Y. Gong, J. Zhang, L. Zhan, L. Ma, Z. Fang, R. Vajtai, X. Wang and P. M. Ajayan, *Adv. Mater.*, 2013, **25**, 2452–2456.
64 F. Wang, Z. Zhang, I. Shakir, C. Yu and Y. Xu, *Adv. Sci.*, 2022, **9**, 2103814.
65 T. Banerjee, F. Podjaski, J. Kröger, B. P. Biswal and B. V. Lotsch, *Nat. Rev. Mater.*, 2021, **6**, 168–190.
66 P. A. Held, H. Fuchs and A. Studer, *Chem.–Eur. J.*, 2017, **23**, 5874–5892.
67 S. Clair and D. G. de Oteyza, *Chem. Rev.*, 2019, **119**, 4717–4776.
68 L. Hou, G. Tang, H. Huang, S. Yin, B. Long, A. Ali, G. Deng and T. Song, *J. Mater. Chem.*, 2022, **10**, 5287–5294.
69 M. Mansha, T. Ahmad, N. Ullah, S. Akram Khan, M. Ashraf, S. Ali, B. Tan and I. Khan, *Chem. Rec.*, 2022, **22**, e202100336.
70 Y. Z. Cheng, X. Ding and B. H. Han, *ChemPhotoChem*, 2021, **5**, 406–417.
71 A. Hayat, M. Sohail, A. El Jery, K. M. Al-Zaydi, S. Raza, H. Ali, Y. Al-Hadeethi, T. A. Taha, I. U. Din, M. A. Khan, M. A. Amin, E. Ghasali, Y. Orooji, Z. Ajmal and M. Z. Ansari, *Mater. Today*, 2023, **64**, 180–208.
72 S. Luo, Z. Zeng, G. Zeng, Z. Liu, R. Xiao, P. Xu, H. Wang, D. Huang, Y. Liu and B. Shao, *J. Mater. Chem.*, 2020, **8**, 6434–6470.
73 Y. Xu, N. Mao, S. Feng, C. Zhang, F. Wang, Y. Chen, J. Zeng and J. X. Jiang, *Macromol. Chem. Phys.*, 2017, **218**, 1700049.
74 Z. Wang, X. Yang, T. Yang, Y. Zhao, F. Wang, Y. Chen, J. H. Zeng, C. Yan, F. Huang and J. Jiang, *ACS Catal.*, 2018, **8**, 8590–8596.
75 R. S. Sprick, B. Bonillo, M. Sachs, R. Clowes, J. R. Durrant, D. J. Adams and A. I. Cooper, *Chem. Commun.*, 2016, **52**, 10008–10011.
76 Y. Zhao, W. Ma, Y. Xu, C. Zhang, Q. Wang, T. Yang, X. Gao, F. Wang, C. Yan and J. Jiang, *Macromolecules*, 2018, **51**, 9502–9508.
77 X. Zhuang, D. Gehrig, N. Forler, H. Liang, M. Wagner, M. R. Hansen, F. Laquai, F. Zhang and X. Feng, *Adv. Mater.*, 2015, **27**, 3789–3796.
78 D. Tan, W. Fan, W. Xiong, H. Sun, Y. Cheng, X. Liu, C. Meng, A. Li and W. Q. Deng, *Macromol. Chem. Phys.*, 2012, **213**, 1435–1440.
79 C. Shu, C. Han, X. Yang, C. Zhang, Y. Chen, S. Ren, F. Wang, F. Huang and J. X. Jiang, *Adv. Mater.*, 2021, **33**, 2008498.
80 S. Wei, G. Zhang and X. Xu, *Appl. Catal., B*, 2018, **237**, 373–381.
81 L. Wang, Y. Wan, Y. Ding, Y. Niu, Y. Xiong, X. Wu and H. Xu, *Nanoscale*, 2017, **9**, 4090–4096.
82 L. Wang, Y. Y. Wan, Y. J. Ding, S. K. Wu, Y. Zhang, X. L. Zhang, G. Q. Zhang, Y. J. Xiong, X. J. Wu, J. L. Yang and H. X. Xu, *Adv. Mater.*, 2017, **29**, 1702428.
83 Q. Huang, L. Guo, N. Wang, X. Zhu, S. Jin and B. Tan, *ACS Appl. Mater. Interfaces*, 2019, **11**, 15861–15868.
84 Q. Zhi, J. Zhou, W. Liu, L. Gong, W. Liu, H. Liu, K. Wang and J. Jiang, *Small*, 2022, **18**, 2201314.
85 S. Wei, J. Wang, Y. Li, Z. Fang, L. Wang and Y. Xu, *Nano Res.*, 2023, **16**, 6753–6770.
86 Y. Li, X. Song, G. Zhang, L. Wang, Y. Liu, W. Chen and L. Chen, *ChemSusChem*, 2022, **15**, e202200901.
87 L. Chen, M. Huang, B. Chen, C. Gong, N. Li, H. Cheng, Y. Chen, Y. Peng and G. Xu, *Chin. Chem. Lett.*, 2022, **33**, 2867–2882.
88 D. N. Bunck and W. R. Dichtel, *J. Am. Chem. Soc.*, 2013, **135**, 14952–14955.
89 G. Li, K. Zhang and T. Tsuru, *ACS Appl. Mater. Interfaces*, 2017, **9**, 8433–8436.
90 S. Chandra, S. Kandambeth, B. P. Biswal, B. Lukose, S. M. Kunjir, M. Chaudhary, R. Babarao, T. Heine and R. Banerjee, *J. Am. Chem. Soc.*, 2013, **135**, 17853–17861.
91 W. Dai, F. Shao, J. Szczerbiński, R. McCaffrey, R. Zenobi, Y. Jin, A. D. Schlüter and W. Zhang, *Angew. Chem., Int. Ed.*, 2016, **128**, 221–225.
92 Y. Li, M. Zhang, X. Guo, R. Wen, X. Li, X. Li, S. Li and L. Ma, *Nanoscale Horiz.*, 2018, **3**, 205–212.
93 E. Jin, Z. Lan, Q. Jiang, K. Geng, G. Li, X. Wang and D. Jiang, *Chem*, 2019, **5**, 1632–1647.
94 Z. Zhou, Y. Xiao, J. Tian, N. Nan, R. Song and J. Li, *J. Mater. Chem. A*, 2023, **11**, 3245–3261.
95 S. Liu, M. Wang, Y. He, Q. Cheng, T. Qian and C. Yan, *Coordin. Chem. Rev.*, 2023, **475**, 214882.
96 X. Li, T. Goto, K. Nomura, M. Zhu, T. Sekino and Y. Osakada, *Appl. Surf. Sci.*, 2020, **513**, 145720.
97 X. Wang, L. Chen, S. Y. Chong, M. A. Little, Y. Wu, W.-H. Zhu, R. Clowes, Y. Yan, M. A. Zwijnenburg and R. S. Sprick, *Nat. Chem.*, 2018, **10**, 1180–1189.
98 K. L. Corp and C. W. Schlenker, *J. Am. Chem. Soc.*, 2017, **139**, 7904–7912.
99 K. Schwinghammer, M. B. Mesch, V. Duppel, C. Ziegler, J. R. Senker and B. V. Lotsch, *J. Am. Chem. Soc.*, 2014, **136**, 1730–1733.
100 Y. Yang, X. Chu, H.-Y. Zhang, R. Zhang, Y.-H. Liu, F.-M. Zhang, M. Lu, Z.-D. Yang and Y.-Q. Lan, *Nat. Commun.*, 2023, **14**, 593.

101 T. Sun, C. Wang and Y. Xu, *Chem. Res. Chin. Univ.*, 2020, **36**, 640–647.
102 Y. Zhu, X. Chen, Y. Cao, W. Peng, Y. Li, G. Zhang, F. Zhang and X. Fan, *Chem. Commun.*, 2019, **55**, 1434–1437.
103 J. Liu, P. Lyu, Y. Zhang, P. Nachtigall and Y. Xu, *Adv. Mater.*, 2018, **30**, 1705401.
104 H. Zhang, W. Sun, X. Chen and Y. Wang, *ACS Nano*, 2019, **13**, 14252–14261.
105 C. Wang, H. Zhang, W. Luo, T. Sun and Y. Xu, *Angew. Chem., Int. Ed.*, 2021, **60**, 25381–25390.
106 T. Sun, Y. Liang and Y. Xu, *Angew. Chem., Int. Ed.*, 2022, **61**, e202113926.
107 T. Sun, S. Li, L. Zhang and Y. Xu, *Angew. Chem., Int. Ed.*, 2023, **62**, e202301865.
108 C. Wang, P. Lyu, Z. Chen and Y. Xu, *J. Am. Chem. Soc.*, 2023, **145**(23), 12745–12754.
109 L. Li, Y. Zhu, N. Gong, W. Zhang, W. Peng, Y. Li, F. Zhang and X. Fan, *Int. J. Hydrogen Energy*, 2020, **45**, 2689–2698.
110 H. Ye, N. Gong, Y. Cao, X. Fan, X. Song, H. Li, C. Wang, Y. Mei and Y. Zhu, *Chem. Mater.*, 2022, **34**, 1481–1490.
111 S. Zhang, G. Cheng, L. Guo, N. Wang, B. Tan and S. Jin, *Angew. Chem., Int. Ed.*, 2020, **59**, 6007–6014.
112 S. Ye, R. Wang, M. Wu and Y. Yuan, *Appl. Surf. Sci.*, 2015, **358**, 15–27.
113 M. Aggarwal, S. Basu, N. P. Shetti, M. N. Nadagouda, E. E. Kwon, Y.-K. Park and T. M. Aminabhavi, *Chem. Eng. J.*, 2021, **425**, 131402.
114 X. Wang, K. Maeda, A. Thomas, K. Takanabe, G. Xin, J. M. Carlsson, K. Domen and M. Antonietti, *Nat. Mater.*, 2009, **8**, 76–80.
115 M. Reli, P. Huo, M. Sihor, N. Ambrozova, I. Troppová, L. Matejova, J. Lang, L. Svoboda, P. Kustrowski and M. Ritz, *J. Phys. Chem. A*, 2016, **120**, 8564–8573.
116 K. Qi, J. Jing, G. Dong, P. Li and Y. Huang, *Environ. Res.*, 2022, **212**, 113405.
117 Y. Shiraishi, S. Kanazawa, Y. Sugano, D. Tsukamoto, H. Sakamoto, S. Ichikawa and T. Hirai, *ACS Catal.*, 2014, **4**, 774–780.
118 X. Zhang, J. Yan, F. Zheng, J. Zhao and L. Y. S. Lee, *Appl. Catal., B*, 2021, **286**, 119879.
119 L. Wang, Y. Hong, E. Liu, X. Duan, X. Lin and J. Shi, *Carbon*, 2020, **163**, 234–243.
120 Q. Xu, B. Zhu, B. Cheng, J. Yu, M. Zhou and W. Ho, *Appl. Catal., B*, 2019, **255**, 117770.
121 J. Jia, W. Sun, Q. Zhang, X. Zhang, X. Hu, E. Liu and J. Fan, *Appl. Catal., B*, 2020, **261**, 118249.
122 W. Xing, W. Tu, Z. Han, Y. Hu, Q. Meng and G. Chen, *ACS Energy Lett.*, 2018, **3**, 514–519.
123 Z. Huang, Y. Zhang, H. Dai, Y. Wang, C. Qin, W. Chen, Y. Zhou and S. Yuan, *J. Catal.*, 2019, **378**, 331–340.
124 X. Zhu, J. Luo, Z. Dong, Z. Li, Y. Wu, Z. Cheng, X. Cao, Y. Wang, Y. Liu and Z. Zhang, *Sep. Purif. Technol.*, 2023, 124235.
125 M. Tahir, C. Cao, N. Mahmood, F. K. Butt, A. Mahmood, F. Idrees, S. Hussain, M. Tanveer, Z. Ali and I. Aslam, *ACS Appl. Mater. Interfaces*, 2014, **6**, 1258–1265.
126 Z. Jiang, X. Zhang, H. S. Chen, X. Hu and P. Yang, *ChemCatChem*, 2019, **11**, 4558–4567.
127 Z. Mo, X. Zhu, Z. Jiang, Y. Song, D. Liu, H. Li, X. Yang, Y. She, Y. Lei and S. Yuan, *Appl. Catal., B*, 2019, **256**, 117854.
128 J. Fu, J. Yu, C. Jiang and B. Cheng, *Adv. Energy Mater.*, 2018, **8**, 1701503.
129 J. Wen, J. Xie, X. Chen and X. Li, *Appl. Surf. Sci.*, 2017, **391**, 72–123.
130 F. He, Z. Wang, Y. Li, S. Peng and B. Liu, *Appl. Catal., B*, 2020, **269**, 118828.
131 Y. Li, X. Li, H. Zhang, J. Fan and Q. Xiang, *J. Mater. Sci. Technol.*, 2020, **56**, 69–88.
132 Y. Xing, X. Wang, S. Hao, X. Zhang, X. Wang, W. Ma, G. Zhao and X. Xu, *Chin. Chem. Lett.*, 2021, **32**, 13–20.
133 S. Patnaik, D. P. Sahoo and K. Parida, *Carbon*, 2021, **172**, 682–711.
134 R. Guo, J. Wang, Z. Bi, X. Chen, X. Hu and W. Pan, *Chemosphere*, 2022, **295**, 133834.
135 A. Hayat, M. Sohail, J. Ali Shah Syed, A. G. Al-Sehemi, M. H. Mohammed, A. A. Al-Ghamdi, T. Taha, H. Salem AlSalem, A. M. Alenad and M. A. Amin, *Chem. Rec.*, 2022, **22**, e202100310.
136 Y. Liu, S. Shen, Z. Li, D. Ma, G. Xu and B. Fang, *Mater. Charact.*, 2021, **174**, 111031.
137 L. Cui, Y. Liu, X. Fang, C. Yin, S. Li, D. Sun and S. Kang, *Green Chem.*, 2018, **20**, 1354–1361.
138 Q. Liu, J. Shen, X. Yu, X. Yang, W. Liu, J. Yang, H. Tang, H. Xu, H. Li and Y. Li, *Appl. Catal., B*, 2019, **248**, 84–94.
139 Q. Zhu, B. Qiu, M. Du, J. Ji, M. Nasir, M. Xing and J. Zhang, *ACS Sustainable Chem. Eng.*, 2020, **8**, 7497–7502.
140 C. Wu, S. Xue, Z. Qin, M. Nazari, G. Yang, S. Yue, T. Tong, H. Ghasemi, F. C. R. Hernandez and S. Xue, *Appl. Catal., B*, 2021, **282**, 119557.
141 M. Zhang, Y. Yang, X. An, J. Zhao, Y. Bao and L. Hou, *J. Hazard. Mater.*, 2022, **424**, 127424.
142 Z. Ma, P. Zhou, L. Zhang, Y. Zhong, X. Sui, B. Wang, Y. Ma, X. Feng, H. Xu and Z. Mao, *Chem. Phys. Lett.*, 2021, **766**, 138335.
143 J. Zhou, J. Xue, Q. Pan, X. Yang, Q. Shen, T. Ma, X. Liu and H. Jia, *J. Photochem. Photobiol. A*, 2019, **372**, 147–155.
144 J. Yan, J. Liu, Y. Sun, D. Ding, C. Wang, L. Sun and X. Li, *Inorg. Chem. Front.*, 2022, **9**, 1423–1433.
145 J. Hong, D. K. Hwang, R. Selvaraj and Y. Kim, *J. Ind. Eng. Chem.*, 2019, **79**, 473–481.
146 Y. Zhong, Z. Li, X. Zhao, T. Fang, H. Huang, Q. Qian, X. Chang, P. Wang, S. Yan, Z. Yu and Z. Zou, *Adv. Funct. Mater.*, 2016, **26**, 7156–7163.
147 L. Wang, X. Zheng, L. Chen, Y. Xiong and H. Xu, *Angew. Chem., Int. Ed.*, 2018, **57**, 3454–3458.
148 Y. Zang, R. Wang, P.-P. Shao, X. Feng, S. Wang, S.-Q. Zang and T. C. Mak, *J. Mater. Chem. A*, 2020, **8**, 25094–25100.
149 P. Dong, A. Zhang, T. Cheng, J. Pan, J. Song, L. Zhang, R. Guan, X. Xi and J. Zhang, *Chin. J. Catal.*, 2022, **43**, 2592–2605.
150 H. Shen, D. Shang, L. Li, D. Li and W. Shi, *Appl. Surf. Sci.*, 2022, **578**, 152024.

151 M. Luo, Q. Yang, W. Yang, J. Wang, F. He, K. Liu, H. Cao and H. Yan, *Small*, 2020, **16**, 2001100.
152 W. Liu, X. Li, C. Wang, H. Pan, W. Liu, K. Wang, Q. Zeng, R. Wang and J. Jiang, *J. Am. Chem. Soc.*, 2019, **141**, 17431–17440.
153 X. Wang, Z. Fu, L. Zheng, C. Zhao, X. Wang, S. Y. Chong, F. McBride, R. Raval, M. Bilton and L. Liu, *Chem. Mater.*, 2020, **32**, 9107–9114.
154 F. Li, D. Wang, Q. Xing, G. Zhou, S. Liu, Y. Li, L. Zheng, P. Ye and J. Zou, *Appl. Catal., B*, 2019, **243**, 621–628.
155 J. Chen, G. Li, N. Lu, H. Lin, S. Zhou and F. Liu, *Mater. Today Chem.*, 2022, **24**, 100832.
156 X. Lan, C. Du, L. Cao, T. She, Y. Li and G. Bai, *ACS Appl. Mater. Interfaces*, 2018, **10**, 38953–38962.
157 J. Li, P. Liu, H. Huang, Y. Li, Y. Tang, D. Mei and C. Zhong, *ACS Sustainable Chem. Eng.*, 2020, **8**, 5175–5183.
158 Z. Zhang, Y. Jiang, Z. Dong, Y. Chu and J. Xu, *Inorg. Chem.*, 2022, **61**, 16028–16037.
159 Y. Jiao, Y. Li, J. Wang, Z. He and Z. Li, *Mol. Catal.*, 2020, **497**, 111223.
160 B. Yang, Z. Wang, J. Zhao, X. Sun, R. Wang, G. Liao and X. Jia, *Int. J. Hydrogen Energy*, 2021, **46**, 25436–25447.
161 J. Fu, Q. Xu, J. Low, C. Jiang and J. Yu, *Appl. Catal., B*, 2019, **243**, 556–565.
162 L. Acharya, G. Swain, B. P. Mishra, R. Acharya and K. Parida, *ACS Appl. Energy Mater.*, 2022, **5**, 2838–2852.
163 B. Xu, X. Fu, X. You, E. Zhao, F. Li, Z. Chen, Y. Li, X. Wang and Y. Yao, *ACS Catal.*, 2022, **12**, 6958–6967.
164 X. She, J. Wu, H. Xu, J. Zhong, Y. Wang, Y. Song, K. Nie, Y. Liu, Y. Yang and M. T. F. Rodrigues, *Adv. Energy Mater.*, 2017, **7**, 1700025.
165 C. Sun, J. Yang, Y. Zhu, M. Xu, Y. Cui, L. Liu, W. Ren, H. Zhao and B. Liang, *J. Alloy. Compd.*, 2021, **871**, 159561.
166 C. Jin, W. Li, Y. Chen, R. Li, J. Huo, Q. He and Y. Wang, *Ind. Eng. Chem. Res.*, 2020, **59**, 2860–2873.
167 A. Kundu, S. Sharma and S. Basu, *J. Phys. Chem. Solids*, 2021, **154**, 110064.
168 M. Wang, P. Guo, Y. Zhang, T. Liu, S. Li, Y. Xie, Y. Wang and T. Zhu, *Appl. Surf. Sci.*, 2018, **453**, 11–22.
169 G. Zhou, J. Yang, X. Zhu, Q. Li, Q. Yu, W. El-alami, C. Wang, Y. She, J. Qian and H. Xu, *J. Energy Chem.*, 2020, **49**, 89–95.
170 S. Tonda, S. Kumar, M. Bhardwaj, P. Yadav and S. Ogale, *ACS Appl. Mater. Interfaces*, 2018, **10**, 2667–2678.
171 M. Sayed, B. Zhu, P. Kuang, X. Liu, B. Cheng, A. A. A. Ghamdi, S. Wageh, L. Zhang and J. Yu, *Adv. Sustainable Syst.*, 2022, **6**, 2100264.
172 B. Tahir, M. Tahir and M. G. Mohd Nawawi, *Energy Fuels*, 2020, **34**, 14400–14418.
173 Y. Bai, L. Wilbraham, B. J. Slater, M. A. Zwijnenburg, R. S. Sprick and A. I. Cooper, *J. Am. Chem. Soc.*, 2019, **141**, 9063–9071.
174 C. Ye, J. Li, Z. Li, X. Li, X. Fan, L. Zhang, B. Chen, C. Tung and L. Wu, *ACS Catal.*, 2015, **5**, 6973–6979.
175 Q. Zhang, X. Chen, Z. Yang, T. Yu, L. Liu and J. Ye, *ACS Appl. Mater. Interface*, 2022, **14**, 3970–3979.
176 Y. Deng, J. Liu, Y. Huang, M. Ma, K. Liu, X. Dou, Z. Wang, S. Qu and Z. Wang, *Adv. Funct. Mater.*, 2020, **30**, 2002353.
177 H. Chen, A. M. Gardner, G. Lin, W. Zhao, M. Bahri, N. D. Browning, R. S. Sprick, X. Li, X. Xu and A. I. Cooper, *Catal. Sci. Technol.*, 2022, **12**, 5442–5452.